This is a peer-reviewed, author's accepted manuscript of the following research article:
Amiri-Hezaveh, A., Moghaddasi, H., & Ostoja-Starzewski, M. (2022). Convolution finite element method for analysis of piezoelectric materials.
Computer Methods in Applied Mechanics and Engineering, 400, [115463].
https://doi.org/10.1016/j.cma.2022.115463

CONVOLUTION FINITE ELEMENT METHOD FOR ANALYSIS OF PIEZOELECTRIC MATERIALS

A PREPRINT

A. Amiri-Hezaveh[1], H. Moghaddasi[2], and M. Ostoja-Starzewski[3]

[1]Department of Mechanical Science and Engineering, University of Illinois at Urbana-Champaign, US
[2]Department of Civil and Environmental Engineering, University of Strathclyde, Glasgow, Scotland, G1 1XQ, UK
[3]Department of Mechanical Science and Engineering, University of Illinois at Urbana-Champaign, US
[3] Institute for Condensed Matter Theory and Beckman Institute, University of Illinois at Urbana-Champaign, US

June 21, 2022

ABSTRACT

A new finite element scheme is proposed to analyze the elastodynamics of materials having interactions between electrical and mechanical fields. Based on coupled constitutive equations and the alternative field equations, a new form of weighted residual in terms of the convolution product is established. Next, the Galerkin formulation is utilized with a particular form of spatial-temporal shape functions. High precision for arbitrary time intervals can be attained by reducing the integral forms to a set of algebraic equations. To show the accuracy of the proposed method, several examples, including elastodynamics of 1d and 2d piezoelectric materials under various initial and boundary conditions are given. The present contribution introduces a new solution procedure for the analysis and design of active materials.

***K*eywords** convolution finite element method · elastodynamics · piezoelectric materials

1 Introduction

The growing use of smart materials in various areas of modern technology necessitates the improvement of available analytical tools. The unique electromechanical properties are the reason for numerous applications, including ultrasonic transducers and micro-actuators, thermal-imaging devices, health monitoring devices, biomedical devices, biomimetics, energy harvesting, micro-wave electronic and optoelectronic instruments [1, 2, 3]. Some notable contributions generalizing the classical continuum mechanics in this area are [4, 5, 6, 7, 8, 9, 10, 11, 12, 13, 14]. Given the complexity posed by the constitutive equations, boundary and initial conditions, and the geometry of the problem domain, one typically relies on numerical methods for partial differential equations to obtain solutions of boundary value problems (BVPs) and initial-boundary value problems (IBVPs). This situation is exacerbated for piezoelectric (piezomagnetic) materials as the equations of motion combined with Maxwell's equations are encountered. For instance, special attention should be paid as constitutive equations relevant to such materials consist of coefficients with different orders of magnitudes. Since the present work focuses on developing a numerical method for analyzing piezoelectric (piezomagnetic) materials, we restrict our attention to numerical studies accomplished for the analysis/design of such materials. A finite element formulation for piezoelectric materials was presented in the seminal work [15], where the piezoelectric effect can be directly inserted in the stiffness matrix, thus leading to a modified problem in classical elastostatics and elastodynamics. Once the displacement field is obtained, one can compute the electrical quantities, i.e., electric potential, electric field, and electric displacement. A similar formulation for piezoelectric actuators and ultrasonic transducers can be found in [16], where the corresponding eigenvalue problems and IBVPs were analyzed under various circumstances. A finite element procedure with transition elements was employed in [17] to address the interaction of 2d structures with 3d piezoelectric devices.
In a different strategy, using the reciprocity, [18] derived an integral boundary equation (BIE) for piezoelectric materials and solved the equation with the boundary element method (BEM). In [19], a new finite element approach was formu-

lated by introducing the electric displacement in terms of a vector potential, allowing handling of nonlinear problems. However, the drawbacks of that method are the computational cost for 3d problems as well as "the inability of the method to account for a free charge density within the material volume."
There is yet another approach, the so-called Trefftz finite element (TFEM), where the physical quantities, i.e., displacement and electric potential, satisfy governing equations in the range of elements. Then, the continuity condition is fulfilled through a variational approach [20]. The particular application of this method for anti-plane problems was then reported in [21]. Hybrid fundamental-solution-based FEM for plane piezoelectric problems was presented in [22]. The idea behind this method is the same as TFEM, while the intra-element fields are calculated based on the fundamental solution. In general, the application of TFEM methods is limited since the intra-element displacement and electric potentials are supposed to satisfy governing equations, which have been carried out either by Stroh formalism or the fundamental solution. As a result, the implementation of the method requires special mathematical techniques.
Interaction of piezoelectric structural-acoustic coupled problems can be found in [23]. The procedure is based on symmetrizing an initially unsymmetrical variation form resulting from governing PDEs. A new form of the mixed variational formulation was proposed in [24] & [25], respectively, for beam and shell piezoelectric structures to remove computational errors due to using lower order interpolation function. The implementation of the NURBS concept for fracture analysis of piezoelectric materials can be found in [26]. The discontinuous Heaviside step functions have been utilized to capture the effect of crack efficiently. In any dynamic analyses, after implementing an appropriate theory, a similar set of ordinary differential equations has been reported. These equations are typically solved through finite difference methods, e.g., the Newmark family of methods. However, in pure elastodynamics, there are numerical methods originating from coupled space-time integral formulations, obtaining more accurate results mainly because of the general superiority of the finite element approaches over the finite difference schemes. As most piezoelectric (piezomagnetic) continuum theories are based on the coupling between mechanical and electrical fields in the constitutive equations, the transformation of the same merit (i.e., gaining arbitrary order of accuracy) is foreseeable for analysis/design of piezoelectric (piezomagnetic) materials. A new type of time-domain finite element method, *convolution finite element method (CFEM)*, based on the alternative governing equations of motion [27], has recently been introduced [28]. While it stems from space-time coupled variational principles, this method preserves the simplicity of time integration methods. Similar variational formulations for electromagneto-elasticity have been established in [29]. Recently, a similar approach has been followed in [30] for a class of nonlinear dynamical systems in which the method, in contrast to the Newmark average acceleration method, adaptively conserves the constants of motion. Hence, it is advantageous to introduce such methods for the case of piezoelectric (piezomagnetic) materials.
In this contribution, the CFEM is developed for piezoelectric materials. As the finite element analysis of linear piezoelectric and piezomagnetic materials has the same form, we only consider the piezoelectricity in this study. Also, we deal with the classical form, in which the stress and electric displacement are written in terms of the strain and electric fields while the electric field is expressed in terms of the electric potential. This method is also applicable to other forms of the finite element formulation, such as the one introduced in [19] and [31]. The outline of the remainder of the paper is as follows: the governing equations of motion of piezoelectric materials are briefly presented. Next, the corresponding alternative formulation is set down, leading to a weak formulation in terms of the convolution product. A particular form of time-space shape functions is adapted for displacement and electric potentials, resulting in a coupled form similar to the time-integration methods. Finally, a comprehensive numerical study is performed to show the power of the method.

2 Definition of the Problem

In this section, the field equations for a piezoelectric material are listed. Throughout the paper, we indicate the position vector and time parameter, respectively, by $\mathbf{x}$ and t. Also, the standard index notation for Cartesian tensors is employed. Let $\bar{V}$ denote a closed and bounded subset of 3D Euclidean space, with interior V and boundary ∂V occupied by a deformable piezoelectric material. Let $u_i(\mathbf{x},t)$, $\sigma_{ij}(\mathbf{x},t)$, $\varepsilon_{ij}(\mathbf{x},t)$, $f_i(\mathbf{x},t)$, $E_i(\mathbf{x},t)$, $D_i(\mathbf{x},t)$ with $(\mathbf{x},t) \in \bar{V} \times (0,T)$, respectively, denote the components of the displacement vector, stress tensor, strain tensor, body force, electric field, electric displacement field. In addition, scalar fields, $\rho(\mathbf{x},t)$, $q_e(\mathbf{x},t)$, and $\varphi(\mathbf{x},t)$ denote the mass density, charge density, and electric potential, respectively.
Let ∂V_{O} denote a subset of ∂V over which $\mathrm{O} = u_i$, $\sigma_{\mathbf{i}}$, φ, and D, are prescribed with the following condition:

$$\begin{aligned} \partial V_{u_i} \cup \partial V_{\sigma_i} = \partial V \quad \partial V_{u_i} \cap \partial V_{\sigma_i} = \emptyset, \\ \partial V_{\varphi} \cup \partial V_{D} = \partial V \quad \partial V_{\varphi} \cap \partial V_{D} = \emptyset, \end{aligned} \tag{2.1}$$

where $i = 1, 2, 3$.
Furthermore, the quasi-static electromagnetic condition is presumed; it is assumed that the electric and magnetic fields are both curl-free. This approximation obtains accurate results, for instance, in the analysis of non-magnetizable elastic dielectrics when the wavelengths of mechanical waves are negligible when compared to wavelengths of electromagnetic

waves of the same frequency [13]. Accordingly, the governing equations read:

$$\begin{aligned} \rho \ddot{u}_i &= \sigma_{ij,j} + F_i \quad on\ \ V \times (0,T), \\ D_{i,i} &= q_e \qquad\quad on\ \ V \times (0,T), \end{aligned} \tag{2.2}$$

in which $\sigma_{ij} = \sigma_{ji}$. Also, the kinematic equations are:

$$\begin{aligned} \varepsilon_{ij} &= u_{(i,j)} = \frac{1}{2}(u_{i,j} + u_{j,i}) \quad on\ \ V \times (0,T), \\ E_i &= -\varphi_{,i} \qquad\qquad\quad on\ \ V \times (0,T), \end{aligned} \tag{2.3}$$

where $u_{(i,j)}$ denotes the symmetric part of the second-order tensor $u_{i,j}$.
Next, the constitutive equations, under the isothermal condition, for a hyper-elastic piezoelectric material read:

$$\begin{aligned} \sigma_{ij} &= C_{ijkl}\varepsilon_{kl} - e^E_{kij}E_k \quad on\ \ V \times (0,T), \\ D_i &= e^E_{ikl}\varepsilon_{kl} + \kappa^E_{ij}E_j \qquad on\ \ V \times (0,T), \end{aligned} \tag{2.4}$$

with symmetry conditions:

$$\begin{aligned} C_{ijkl} &= C_{klij} = C_{jikl} = C_{ijlk} \quad on\ \ V, \\ e^E_{kij} &= e^E_{kji},\ \kappa^E_{ij} = \kappa^E_{ji} \qquad\quad on\ \ V. \end{aligned} \tag{2.5}$$

where the coefficients C_{ijkl}, e^E_{kij} and κ^E_{ij}, all functions of the position, represent components of the stiffness tensor, piezoelectric tensor, and permittivity tensor under constant strain, respectively. Next, to form the IBVP, we define the boundary conditions:

$$\begin{aligned} &\text{mechanical boundary conditions} \begin{cases} u_i = \hat{u}_i(\mathbf{x},t) & on\, \partial V_{u_i} \times (0,T), \\ t_i = \hat{t}_i(\mathbf{x},t) & on\, \partial V_{\sigma_{\mathbf{i}}} \times (0,T), \end{cases} \\ &\text{electric boundary conditions} \quad \begin{cases} \varphi = \hat{\varphi}(\mathbf{x},t) & on\, \partial V_{\varphi} \times (0,T), \\ d = \hat{d}(\mathbf{x},t) & on\, \partial V_D \times (0,T), \end{cases} \end{aligned} \tag{2.6}$$

and the initial conditions:

$$\begin{aligned} u_i(\mathbf{x},0) &= u^0_i(\mathbf{x}) \quad \mathbf{x} \in \bar{V}, \\ \dot{u}_i(\mathbf{x},0) &= v^0_i(\mathbf{x}) \quad \mathbf{x} \in \bar{V}. \end{aligned} \tag{2.7}$$

where $t_i = \sigma_{ij}n_j$, and $d = D_i n_i$.
Alternatively, satisfaction of equations of motion and initial conditions are secured when the following holds [27]:

$$\rho\mathbf{u}(\mathbf{x},t) = [t * (\nabla.\boldsymbol{\sigma} + \rho\mathbf{f})](\mathbf{x},t) + \rho(\mathbf{u}^0(\mathbf{x}) + t\mathbf{v}^0(\mathbf{x})), \tag{2.8}$$

in which

$$[f * g](\mathbf{x},t) = \int_0^t f(\mathbf{x},t-\tau)g(\mathbf{x},\tau)d\tau. \tag{2.9}$$

Hence, in what follows, (2.8) is used in lieu of original equations motion $(2.2)_1$ and initial conditions (2.7).

3 Convolution Weak Form

This section defines a new type of integral form, which is closely similar to the weighted residual expressed in the classical finite element method. Since this form is based on the alternative formulation (a set of integro-partial differential equations (2.8), which contains time integration in terms of convolution product, we call this form convolution weighted residual. In this regard, in view of Remark 1, one can write:

$$\begin{aligned} \int_V \left[\rho u_i * w_i\right](\mathbf{x},T)dV &= \int_V \left[t * (\sigma_{ij,j} + \rho f_i) * w_i\right](\mathbf{x},T)dV + \int_V \left[\rho(u^0_i + tv^0_i) * w_i\right](\mathbf{x},T)dV, \\ \int_V \left[D_{i,i} * w^E\right](\mathbf{x},T)dV &= \int_V \left[q_e * w^E\right](\mathbf{x},T)dV \end{aligned} \tag{3.1}$$

in which w_i and w^E are the weighting functions corresponding to displacement and electric potential, and the following notation has been used:

$$[f*g*h](\mathbf{x},t)=\int_0^t\left(\int_0^\lambda f(\mathbf{x},\lambda-\tau)g(\mathbf{x},\tau)d\tau\right)h(\mathbf{x},t-\lambda)d\lambda. \tag{3.2}$$

Lemma 1 implies that (2.2) is satisfied in the sense of (A.5) provided that (3.1) is met for all displacement and electric potential weight functions (i.e., for every w_i and w^E). As discussed in Appendix A, the multiplications of the aforementioned weight functions can also be done in terms of the dot product. However, since the convolution form resembles the convolutional variational forms, the one with convolution product is pursued in this work. To proceed, we define solution and variation spaces:

Definition 1. *$\mathbb{S}_i$ ($\mathbb{S}^{\mathbb{E}}$) and $\mathbb{V}_i$ ($\mathbb{V}^{\mathbb{E}}$) stand for, respectively, the solution space and the variation space whose elements have the following properties:*

$$\begin{aligned}\mathbb{S}_i&=\{u_i\in L^2(0,T;\mathrm{H}^1(V))|\,u_i=\hat{u}_i(\mathbf{x},t)\text{ on }\partial V_{u_i}\times(0,T)\},\\ \mathbb{S}^{\mathbb{E}}&=\{\varphi\in L^2(0,T;\mathrm{H}^1(V))|\varphi=\hat{\varphi}(\mathbf{x},t)\text{ on }\partial V_{\varphi}\times(0,T)\},\end{aligned} \tag{3.3}$$

$$\begin{aligned}\mathbb{V}_i&=\{w_i\in L^2(0,T;\mathrm{H}^1(V))|\,w_i=0\text{ on }\partial V_{u_i}\times(0,T)\},\\ \mathbb{V}^{\mathbb{E}}&=\{w^E\in L^2(0,T;\mathrm{H}^1(V))|w^E=0\text{ on }\partial V_{\varphi}\times(0,T)\},\ i=1,2,3.\end{aligned} \tag{3.4}$$

Assuming $u_i\in\mathbb{S}_i$ ($\varphi\in\mathbb{S}^{\mathbb{E}}$) and $w_i\in\mathbb{V}_i$ ($w^{\mathbb{E}}\in\mathbb{V}^{\mathbb{E}}$), employing (2.4), applying divergence theorem, one can write(3.1)as:

$$\begin{aligned}&\int_V\left[\rho u_i*w_i\right](\mathbf{x},T)dV+\int_V\left[t*(C_{ijkl}u_{i,j}+e^E_{ikl}\varphi_{,i})*w_{k,l}\right](\mathbf{x},T)dV=\\ &\sum_{i=1}^3\int_{\partial V_{\sigma_i}}\left[t*\hat{t}_i*w_i\right](\mathbf{x},T)d\Gamma+\int_V\left[t*\rho f_i*w_i\right](\mathbf{x},T)dV+\int_V\left[\rho(u_i^0+tv_i^0)*w_i\right](\mathbf{x},T)dV,\\ &\int_V\left[(e^E_{ikl}u_{k,l}-\kappa^E_{ij}\varphi_{,j})*w^E_{,i}\right](\mathbf{x},T)dV=\int_{\partial V_D}\left[\hat{d}*w^E\right](\mathbf{x},T)dV-\int_V\left[q_e*w^E\right](\mathbf{x},T)dV,\end{aligned} \tag{3.5}$$

Now, we are able to define a weak solution:

Definition 2. *Let u_i and φ be an element of $\mathbb{S}_i$ and $\mathbb{S}^{\mathbb{E}}$, respectively. Then, the ordered array $S=[\mathbf{u},\varphi]$ is called a weak solution if (3.5) is satisfied for all $w_i\in\mathbb{V}_i$ and $w^{\mathbb{E}}\in\mathbb{V}^{\mathbb{E}}$.*

Now, because of the results given in Appendix A, it is a classical practice to show that the weak and strong solutions are equivalent:

Theorem 1. *Let all the necessary conditions validating the derivation of (3.5) hold. Then, the weak and displacement-potential strong solutions are equivalent.*

4 Convolution Galerkin Formulation

Galerkin formulation corresponding to (3.5) is introduced in this section. Similar to the classical finite element method, we write u_i^h and φ^h,respectively, an element of $\mathbb{S}_i$ and $\mathbb{S}^{\mathbb{E}}$, in the following form:

$$\begin{aligned}u_i^h(\mathbf{x},t)&=v_i^h(\mathbf{x},t)+\tilde{u}_i^h(\mathbf{x},t),\\ \varphi^h(\mathbf{x},t)&=\bar{\varphi}^h(\mathbf{x},t)+\tilde{\varphi}^h(\mathbf{x},t)\end{aligned} \tag{4.1}$$

with

$$\begin{aligned}v_i^h(\mathbf{x},t)&=0 &&on\quad\partial V_{u_i}\times(0,T),\\ \tilde{u}_i^h(\mathbf{x},t)&=\hat{u}_i(\mathbf{x},t) &&on\quad\partial V_{u_i}\times(0,T),\\ \bar{\varphi}^h(\mathbf{x},t)&=0 &&on\quad\partial V_{\varphi}\times(0,T),\\ \tilde{\varphi}^h(\mathbf{x},t)&=\hat{\varphi}(\mathbf{x},t) &&on\quad\partial V_{\varphi}\times(0,T).\end{aligned} \tag{4.2}$$

Employing (4.1) in (3.5), we obtain:

$$\begin{aligned}
&\int_V \left[\rho v_i^h * w_i\right](\mathbf{x},T)dV + \int_V \left[t*(C_{ijkl}v_{i,j}^h + e_{ikl}^E\bar{\varphi}_{,i}^h)*w_{k,l}\right](\mathbf{x},T)dV = \\
&-\int_V \left[t*(C_{ijkl}\tilde{u}_{i,j}^h + e_{ikl}^E\tilde{\varphi}_{,i}^h)*w_{i,j}\right](\mathbf{x},T)dV - \int_V \left[\rho\tilde{u}_i^h * w_i\right](\mathbf{x},T)dV \\
&+\sum_{i=1}^{3}\int_{\partial V_{\sigma_i}} [t*\hat{t}_i*w_i](\mathbf{x},T)dS + \int_V [t*\rho f_i*w_i](\mathbf{x},T)dV + \int_V \left[\rho(u_i^0+tv_i^0)*w_i\right](\mathbf{x},T)dV, \\
&\int_V \left[(-e_{ikl}^E v_{k,l}^h + \kappa_{ij}^E\varphi_{,j})*w_{,i}^E\right](\mathbf{x},T)dV = \int_V \left[(e_{ikl}^E\tilde{u}_{k,l}^h - \kappa_{ij}^E\tilde{\varphi}_{,j}^h)*w_{,i}^E\right](\mathbf{x},T)dV - \int_{\partial V_D}\left[\hat{d}*w^E\right](\mathbf{x},T)dS \\
&+\int_V \left[q_e*w^E\right](\mathbf{x},T)dV,
\end{aligned} \tag{4.3}$$

where w_i (w^E) and v_i^h (φ^h) are elements of $\mathbb{V}_i$ ($\mathbb{V}^{\mathbb{E}}$). Alternatively, the above form can be rearranged as:

$$\begin{aligned}
&\int_V \left[\rho\mathscr{V}_i^h * w_i\right](\mathbf{x},T)dV + \int_V \left[t*(C_{ijkl}\mathscr{V}_{i,j}^h + e_{ikl}^E\bar{\varphi}_{,i}^h)*w_{k,l}\right](\mathbf{x},T)dV = \\
&-\int_V \left[t*(C_{ijkl}g_{i,j}^h + e_{ikl}^E\tilde{\varphi}_{,i}^h)*w_{k,l}\right](\mathbf{x},T)dV - \int_V \left[t*C_{ijkl}(\tilde{u}_{i,j}^0 + tv_{i,j}^0)*w_{i,j}\right](\mathbf{x},T)dV \\
&-\int_V \left[\rho g_i^h * w_i\right](\mathbf{x},T)dV + \sum_{i=1}^{3}\int_{\partial V_{\sigma_i}} [t*\hat{t}_i*w_i](\mathbf{x},T)dS + \int_V [t*\rho f_i*w_i](\mathbf{x},T)dV, \\
&\int_V \left[(-e_{ikl}^E\mathscr{V}_{k,l}^h + \kappa_{ij}^E\varphi_{,j}^h)*w_{,i}^E\right](\mathbf{x},T)dV = -\int_V \left[\kappa_{ij}^E\tilde{\varphi}_{,j}^h * w_{,i}^E\right](\mathbf{x},T)dV - \int_{\partial V_D}\left[\hat{d}*w^E\right](\mathbf{x},T)dS \\
&+\int_V \left[q_e*w^E\right](\mathbf{x},T)dV + \int_V \left[e_{ikl}^E(u_{k,l}^0(\mathbf{x}) + tv_{k,l}^0(\mathbf{x}) + g_{k,l}^h(\mathbf{x},t))*w_{,i}^E\right](\mathbf{x},T)dV,
\end{aligned} \tag{4.4}$$

where

$$\mathscr{V}_i^h(\mathbf{x},t) = u_i^h(\mathbf{x},t) - u_i^0(\mathbf{x}) - tv_i^0(\mathbf{x}) - g_i^h(\mathbf{x},t), \tag{4.5}$$

in which $g_i^h(\mathbf{x},t)$ satisfies:

$$\begin{aligned}
&g_i^h(\mathbf{x},t) = \hat{u}_i(\mathbf{x},t) - u_i^0(\mathbf{x}) - tv_i^0(\mathbf{x}) \qquad on \quad \partial V_{u_i}\times(0,T), \\
&g_i^h(\mathbf{x},0) = \dot{g}_i^h(\mathbf{x},0) \qquad on \quad \bar{V}.
\end{aligned} \tag{4.6}$$

The homogeneous initial and boundary conditions are required for $\mathscr{V}_i^h(\mathbf{x},t)$. That is:

$$\begin{aligned}
&\mathscr{V}_i^h(\mathbf{x},0) = 0 \qquad on \quad V, \\
&\dot{\mathscr{V}}_i^h(\mathbf{x},0) = 0 \qquad on \quad V, \\
&\mathscr{V}_i^h(\mathbf{x},t) = 0 \qquad on \quad \partial V_{u_i}\times(0,T).
\end{aligned} \tag{4.7}$$

To proceed, analogously to pure elastodynamics [29], $\mathbb{V}_i^{h,x}$ ($\mathbb{V}^{h,E,x}$) denotes the finite dimensional subsets of $\mathrm{H}_0^1(V)$. Also, finite function spaces $\mathbb{V}_i^{h,N}$ and $\mathbb{V}^{h,E,N}$ are defined as:

$$\mathbb{V}_i^{h,N} = \mathbb{V}_i^{h,x}\otimes\mathbb{F}_N^{h,t}, \quad \mathbb{V}^{h,E,N} = \mathbb{V}^{h,x}\otimes\mathbb{F}_N^{h,t}, \tag{4.8}$$

with

$$\mathbb{F}_N^{h,t} = \left\{1, \cos\frac{\pi t}{T}, ..., \cos\frac{(N-1)\pi t}{T}\right\}. \tag{4.9}$$

Although different forms of spatial shape functions are possible, in this study, we present the result for the Lagrangian shape functions [32]. In this regard, let $\eta = \{1,2,...,n_{np}\}$ denote the set of all nodal points specifying the discretized

domain of the problem. Also, η_{gi} and η_g^E stands for the set of all nodal points on the boundary ∂V_{u_i} and ∂V_φ, respectively. Then, $\mathscr{V}_i^h$ and $\bar{\varphi}^h$—elements of, respectively, $\mathbb{V}_i$ and $\mathbb{V}^{\mathbb{E}}$ — can be approximated in terms of elements of $\mathbb{V}_i^{h,N}$ and $\mathbb{V}^{h,E,N}$:

$$\begin{aligned}
\boldsymbol{\mathscr{V}}^h(\mathbf{x},t) &\approx \sum_{P=0}^{N-1}\sum_{j=1}^{n_{dof}}\sum_{\lambda\in\eta-\eta_{gj}} c_{Pj\lambda}\,\psi_\lambda(\mathbf{x})\cos(\frac{P\pi t}{T})\mathbf{e}_j,\\
\bar{\varphi}^h(\mathbf{x},t) &\approx \sum_{P=0}^{N-1}\sum_{\alpha\in\eta-\eta_g^E} c_{P\alpha}^E\,\psi_\alpha(\mathbf{x})\cos(\frac{P\pi t}{T}),
\end{aligned} \tag{4.10}$$

where ψ_α's denote Lagrangian shape functions, $c_{Pj\alpha}$'s and $c_{P\alpha}^E$'s are unknown coefficients to be determined from (4.4), and $\mathbf{e}_j,\ j=1,2,3$, denotes unit vectors of Cartesian coordinate. It is noticed that $(4.10)_1$ satisfies $(4.7)_{2-3}$ while satisfaction of $(4.7)_1$ is ensured by increasing N. Also, the same function space has been considered for both electrical and displacement fields although different spaces can be used. Analogously, we use the following approximation:

$$\begin{aligned}
\mathbf{f}(\mathbf{x},t) &\approx \sum_{P=0}^{N-1}\mathbf{f}_P^c(\mathbf{x})\cos(\frac{P\pi t}{T}), \quad \mathbf{g}^h(\mathbf{x},t) \approx \sum_{P=0}^{N-1}\sum_{j=1}^{n_{dof}}\sum_{\alpha\in\eta-\eta_{gj}} g_{Pj\alpha}^c\,\psi_\alpha(\mathbf{x})\cos(\frac{P\pi t}{T})\mathbf{e}_j,\\
\hat{\mathbf{t}}(\mathbf{x},t) &\approx \sum_{P=0}^{N-1}\mathbf{t}_p^c(\mathbf{x})\cos(\frac{P\pi t}{T}), \quad \tilde{\varphi}^h(\mathbf{x},t) \approx \sum_{P=0}^{N-1}\sum_{\alpha\in\eta_g^E}\tilde{\varphi}_{p\alpha}^c\,\psi_\alpha(\mathbf{x})\cos(\frac{P\pi t}{T}),\\
\hat{d}(\mathbf{x},t) &\approx \sum_{P=0}^{N-1}\hat{d}_p^c(\mathbf{x})\cos(\frac{P\pi t}{T}), \quad q_e(\mathbf{x},t) \approx \sum_{P=0}^{N-1}q_p^c(\mathbf{x})\cos(\frac{P\pi t}{T}),
\end{aligned} \tag{4.11}$$

and the Galerkin form is realized when

$$\mathbf{w}(\mathbf{x},t) \approx \sum_{Q=0}^{N-1}\sum_{i=1}^{n_{dof}}\sum_{\beta\in\eta-\eta_{gi}} d_{Qi\beta}\,\psi_\beta(\mathbf{x})\cos(\frac{Q\pi t}{T})\mathbf{e}_i, \quad w^E(\mathbf{x},t) \approx \sum_{Q=0}^{N-1}\sum_{\beta\in\eta-\eta_g^E} d_{Q\beta}^E\,\psi_\beta(\mathbf{x})\cos(\frac{Q\pi t}{T}). \tag{4.12}$$

4.1 Algebraic Equations

Now, a substitution of (4.10), (4.11), and (4.12) into (4.4) leads us to the following algebraic equations:

$$\begin{aligned}
&\sum_{P=0}^{N-1}\sum_{j=1}^{n_{dof}}\sum_{\alpha\in\eta-\eta_{gj}} c_{Pj\alpha}\left[\mathscr{F}_{PQ}(\rho\,\psi_\alpha\mathbf{e}_j,\psi_\beta\mathbf{e}_i)_V+\mathscr{A}_{PQ}a(\psi_\alpha\mathbf{e}_j,\psi_\beta\mathbf{e}_i)\right]+\sum_{P=0}^{N-1}\sum_{\alpha\in\eta-\eta_g^E}c_{P\alpha}^E\mathscr{A}_{PQ}b(\psi_\alpha,\psi_\beta\mathbf{e}_i)=\\
&-\sum_{P=0}^{N-1}\sum_{j=1}^{n_{dof}}\sum_{\alpha\in\eta_{gj}} g_{Pj\alpha}^c\left[\mathscr{F}_{PQ}(\rho\,\psi_\alpha\mathbf{e}_j,\psi_\beta\mathbf{e}_i)_V+\mathscr{A}_{PQ}a(\psi_\alpha\mathbf{e}_j,\psi_\beta\mathbf{e}_i)\right]-\sum_{P=0}^{N-1}\sum_{\alpha\in\eta_g^E}\tilde{\varphi}_{P\alpha}^c\mathscr{A}_{PQ}b(\psi_\alpha,\psi_\beta\mathbf{e}_i)\\
&+\sum_{P=0}^{N-1}\mathscr{A}_{PQ}\left[(\mathbf{t}_P^c,\psi_\beta\mathbf{e}_i)_{\partial V_\sigma}+(\rho\mathbf{f}_P^c,\psi_\beta\mathbf{e}_i)_V\right]+\mathscr{A}_{0Q}a(\mathbf{u}^0,\psi_\beta\mathbf{e}_i)\\
&+\mathscr{E}_Q\,a(\mathbf{v}^0,\psi_\beta\mathbf{e}_i),\ (i=1,...,n_{dof}),\ (Q=0,...,N-1),\ (\beta\in\eta-\eta_{gi}),\\
&-\sum_{P=0}^{N-1}\sum_{j=1}^{n_{dof}}\sum_{\alpha\in\eta_{gj}} c_{Pj\alpha}\left[\mathscr{F}_{PQ}b(\psi_\beta,\psi_\alpha\mathbf{e}_j)\right]+\sum_{P=0}^{N-1}\sum_{\alpha\in\eta_g^E}c_{P\alpha}^E\left[\mathscr{F}_{PQ}b^E(\psi_\alpha,\psi_\beta)\right]\\
&=-\sum_{P=0}^{N-1}\sum_{\alpha\in\eta_g^E}\tilde{\varphi}_{P\alpha}^c\left[\mathscr{F}_{PQ}b^E(\psi_\alpha,\psi_\beta)\right]+\sum_{P=0}^{N-1}\sum_{j=1}^{n_{dof}}\sum_{\alpha\in\eta_{gi}} g_{Pj\alpha}^c\left[\mathscr{F}_{PQ}b(\rho\,\psi_\alpha\mathbf{e}_j,\psi_\beta)\right]-\sum_{P=0}^{N-1}\mathscr{F}_{PQ}(\hat{d}_P^c,\psi_\beta)_{\partial V_\mathbf{D}}\\
&+\sum_{P=0}^{N-1}\mathscr{F}_{PQ}(q_P^c,\psi_\beta)_V+\mathscr{C}_Q b(\mathbf{u}^0,\psi_\beta)+\mathscr{D}_Q b(\mathbf{v}^0,\psi_\beta),\ (Q=0,...,N-1),\ (\beta\in\eta-\eta_g^e),
\end{aligned} \tag{4.13}$$

in which

$$
\begin{aligned}
\mathscr{A}_{ij} &= t*\cos(\frac{i\pi t}{T})*\cos(\frac{j\pi t}{T})\Big|_{t=T} = \begin{cases} \frac{T^3}{i^2\pi^2} & i\neq 0, j=0 \\ \frac{T^3}{j^2\pi^2} & i=0,\ j\neq 0 \\ (-1)^{i+1}\frac{T^3}{2i^2\pi^2} & i=j\neq 0 \\ \frac{T^3}{6} & i=j=0 \\ 0 & otherwise \end{cases}, \\
\mathscr{C}_i &= 1*\cos(\frac{i\pi t}{T})\Big|_{t=T} = \begin{cases} 0 & i\neq 0 \\ T & i=0 \end{cases}, \\
\mathscr{D}_i &= t*\cos(\frac{i\pi t}{T})\Big|_{t=T} = \begin{cases} -\frac{T^2(-1+(-1)^i)}{i^2\pi^2} & i\neq 0 \\ \frac{T^2}{2} & i=0 \end{cases}, \\
\mathscr{E}_i &= t*t*\cos(\frac{i\pi t}{T})\Big|_{t=T} = \begin{cases} -\frac{T^4\left(2+2(-1)^{m-1}-i^2\pi^2\right)}{2i^4\pi^4} & i\neq 0 \\ \frac{T^4}{24} & i=0 \end{cases}, \\
\mathscr{F}_{ij} &= \cos(\frac{i\pi t}{T})*\cos(\frac{j\pi t}{T})\Big|_{t=T} = \begin{cases} (-1)^i\frac{T}{2} & i=j\neq 0 \\ T & i=j=0 \\ 0 & otherwise \end{cases},
\end{aligned}
\tag{4.14}
$$

where the following notations have been utilized:

$$
\begin{aligned}
&a(\mathbf{u},\mathbf{w}) = \int_V C_{ijkl}u_{i,j}w_{k,l}\,dV, \quad b(\varphi,\mathbf{w}) = \int_V e^E_{ijk}\varphi_{,i}w_{j,k}\,dV, \\
&b^E(\varphi,\widehat{\varphi}) = \int_V \kappa^E_{ij}\varphi_{,i}\widehat{\varphi}_j\,dV, \qquad (\mathbf{u},\mathbf{w})_V = \int_V u_iw_i\,dV, \\
&(\mathbf{u},\mathbf{w})_{\partial V_\sigma} = \sum_{i=1}^{n_{dof}}\int_{\partial V_\sigma} u_iw_i\,d\Gamma, \quad (\varphi,\widehat{\varphi})_{\partial V_{\mathbf{D}}} = \int_{\partial V_{\mathbf{D}}}\varphi\widehat{\varphi}\,dV,
\end{aligned}
\tag{4.15}
$$

for all vectors $\mathbf{u}$ and $\mathbf{w}$, and scalars φ and $\widehat{\varphi}$. n_{dof} indicates number of degree of freedom, which could be $n_{dof}=1,2,3$. It is noted that some of the coefficients (4.14) can be obtained one from another. (4.13) has following matrix form:

$$
\sum_{P=0}^{N-1}\Big(\mathscr{F}_{PQ}\begin{bmatrix}[\mathbf{M}] & [\mathbf{0}]\\ [\mathbf{0}] & [\mathbf{0}]\end{bmatrix} + \begin{bmatrix}\mathscr{A}_{PQ}[\mathbf{K}]_M & \mathscr{A}_{PQ}[\mathbf{K}]_{ME}\\ -\mathscr{F}_{PQ}[\mathbf{K}]^T_{ME} & \mathscr{F}_{PQ}[\mathbf{K}]_E\end{bmatrix}\Big)\begin{bmatrix}[\mathbf{c}]_P\\ [\mathbf{c}]^E_P\end{bmatrix} = \begin{bmatrix}[\mathbf{f}^M_{eq}]\\ [\mathbf{f}^E_{eq}]\end{bmatrix}_Q, Q=0,...,N-1, \tag{4.16}
$$

in which $[\mathbf{f}_{eq}]_Q$ represents the matrix form of the right-hand-side of (4.13):

$$
\begin{aligned}
\left[\mathbf{f}^M_{eq}\right]_Q =& -\sum_{P=0}^{N-1}(\mathscr{F}_{PQ}[\mathbf{M}]+\mathscr{A}_{PQ}[\mathbf{K}]_M)[\mathbf{g}]_P - \sum_{P=0}^{N-1}\mathscr{A}_{PQ}[\mathbf{K}]_{ME}[\tilde{\varphi}]_P + \sum_{P=0}^{N-1}\mathscr{A}_{PQ}[\mathbf{t}]_P + \sum_{P=0}^{N-1}\mathscr{A}_{PQ}[\mathbf{f}]_P \\
&- \mathscr{A}_{0Q}[\mathbf{K}]_M[\mathbf{u}^0] - \mathscr{E}_Q[\mathbf{K}]_M[\mathbf{v}^0], \\
\left[\mathbf{f}^E_{eq}\right]_Q =& \sum_{P=0}^{N-1}\mathscr{F}_{PQ}[\mathbf{K}]^T_{ME}[\mathbf{g}]_P - \sum_{P=0}^{N-1}\mathscr{F}_{PQ}[\mathbf{K}]_E[\tilde{\varphi}]_P + \sum_{P=0}^{N-1}\mathscr{F}_{PQ}[\mathbf{q}]_P - \sum_{P=0}^{N-1}\mathscr{F}_{PQ}[\mathbf{d}]_P \\
&+ \mathscr{C}_Q[\mathbf{K}]^T_{ME}[\mathbf{u}^0] + \mathscr{D}_Q[\mathbf{K}]^T_{ME}[\mathbf{v}^0].
\end{aligned}
\tag{4.17}
$$

$[\mathbf{M}]$, $[\mathbf{K}]_M$, $[\mathbf{K}]_{ME}$, $[\mathbf{K}]_E$, $[\mathbf{t}]_p$, $[\mathbf{f}]_P$, $[\mathbf{q}]_P$, and $[\mathbf{d}]_P$ are matrices defined in the classical FEM (see [32] and [15] for more details). As the matrix $[\mathscr{F}]$ is diagonal, one can obtain a condense form of(4.16) as follows:

$$
\begin{aligned}
&\sum_{P=0}^{N-1}((\mathscr{F}_{PQ}[\mathbf{M}]+\mathscr{A}_{PQ}([\mathbf{K}]_M+[\mathbf{K}]_{ME}[\mathbf{K}]^{-1}_E[\mathbf{K}]^T_{ME}))[\mathbf{c}]_P = \left[\mathbf{f}^M_{eq}\right]_Q - \sum_{P=0}^{N-1}\mathscr{A}_{PQ}[\mathbf{K}]_{ME}[\mathbf{K}]^{-1}_E\left[\mathbf{f}^E_{eq}\right]_P \\
&, Q=0,...,N-1.
\end{aligned}
\tag{4.18}
$$

Solving the set of algebraic equations (4.18), one can obtain the displacement field from (4.5), (4.6) and (4.10). Also, the coefficients $[\mathbf{c}]^E_P$'s are obtained from

$$
[\mathbf{c}]^E_P = [\mathbf{K}]^{-1}_E[\mathbf{K}]^T_{ME}[\mathbf{c}]_P,\ P=0,...,N-1, \tag{4.19}
$$

upon which one can obtain electric potential from $(4.10)_2$ and $(4.1)_2$. Other physical quantities— namely, velocity, acceleration, and electric field— can then be found from the spatial and time derivatives of the displacement and electric potential fields. It is noticed that analogous to [15] the study of the elastodynamics of piezoelectric materials has degenerated to elastodynamics of non-piezoelectric material resulting in the modified stiffness matrix:

$$\left[\tilde{\mathbf{K}}\right]_{\mathrm{mo}} = [\mathbf{K}]_M + [\mathbf{K}]_{ME}[\mathbf{K}]_E^{-1}[\mathbf{K}]_{ME}^T, \tag{4.20}$$

combined with (4.19). Indeed, from the similar procedure represented in [28], which stems from the semi-discretized equations of motion, one can revisit (4.18) (see [28], section 5). Apparently, (4.18) is a set of algebraic equations whose size is N times of the similar elastostatics problem. However, by considering (4.14) and (4.18), one can find that the left-hand-side coefficients form a block arrowhead matrix that leads to avoiding direct calculation of the inverse matrix. As a result, to find the unknowns, one can implement the algorithm mentioned in [28].
Furthermore, as introduced in [19], there is another finite element formulation corresponding to the analysis of piezoelectric materials in which the electric field is expressed in terms of vector potential function rather than a scalar one. After introducing spatial shape functions, this formulation yields a similar but conceptually different system of ODEs if compared to the standard format. Hence, by considering the alternative derivation of the CFEM mentioned in [28], section 5, we notice that the above method can be successfully adapted for the case of vector electric potential function as well. Moreover, by the same analogy, one can see the above formulation can be developed for the framework given in [31].

5 Numerical Analysis

The proposed framework is numerically investigated in this section. In this regard, several initial-boundary value problems are considered.

5.1 1d Cases

First, the elastodynamics of a piezoelectric bar is simulated, and the corresponding solution are compared with the one resulting from the separation of variables (see appendix B). The bar has the length of L with an arbitrary cross-section, which is small in comparison to the length of the bar (See Fig. 2). The mechanical boundary conditions are

$$\begin{aligned} u_3(0,t) &= 0, \\ \sigma_{33}(L,t) &= \hat{\sigma}_{33}, \end{aligned} \tag{5.1}$$

where $\hat{\sigma}_{33}$ is the vertical traction applied at $x = L$. For the electrical field, two sets of boundary conditions are assumed. In the first case, a Dirichlet boundary condition is considered:

$$\begin{aligned} \varphi(0,t) &= V_1, \\ \varphi(L,t) &= V_2, \end{aligned} \tag{5.2}$$

where V_1 and V_2 are electrical potential imposed at $x = 0$ and $x = L$, respectively. In the second case, a mixed boundary condition is set:

$$\begin{aligned} \varphi(0,t) &= V_1, \\ D_3(L,t) &= \hat{d}_3, \end{aligned} \tag{5.3}$$

where $\hat{d}_3$ is the electric flux imposed at $x = L$. For both cases, the following initial conditions are assumed:

$$\begin{aligned} u_3(x_3,0) &= u_3^0, \\ \dot{u}_3(x_3,0) &= v_3^0, \end{aligned} \tag{5.4}$$

The PZT-5h is selected as the piezoelectric material (see table 1). The numerical values of the above-mentioned parameters are $\hat{\sigma}_{33} = 0, V_1 = 0, V_2 = 200V,\ \hat{d}_3 = -0.01Cm^{-2}$.

Homogeneous initial data are applied for the first case (i.e., $u_3^0 = 0,\ v_3^0 = 0$), while a non-trivial velocity field $v_3^0 = 0.1\mathrm{m/s}$ is presumed with homogeneous initial displacement for the second case. Linear Lagrangian shape functions are utilized for spatial discretization.
For the first case in Figs. 3 & 4, the displacement of the bar at $x = L/2$ has been determined with the new method and compared to the analytical solution developed in Appendix B. In these Figures, 10 and 100 elements are utilized for spatial discretization, respectively. As shown in [28], one should increase the number of time-wise terms when finer spatial meshes are utilized. Hence, we considered $N = 20$ and $N = 2000$, respectively, for 10 and 100 elements. It is evident that the analytical solutions can be recovered satisfactorily if the number of elements and time-wise terms

Materials' Properties											
Mat	C_{11} $(\frac{N}{m^2})$	C_{12} $(\frac{N}{m^2})$	C_{13} $(\frac{N}{m^2})$	C_{33} $(\frac{N}{m^2})$	C_{44} $(\frac{N}{m^2})$	e_{13} $(\frac{C}{m^2})$	e_{33} $(\frac{C}{m^2})$	e_{15} $(\frac{C}{m^2})$	κ_{11} $(\frac{C}{Nm})$	κ_{33} $(\frac{C}{Nm})$	ρ $(\frac{Kg}{m^3})$
PZT-5h	12.6×10^{10}	7.95×10^{10}	8.39×10^{10}	11.7×10^{10}	2.3×10^{10}	-6.5	23.3	17	15×10^{-9}	13×10^{-9}	7500
PZT-4h	12.6×10^{10}	7.78×10^{10}	7.43×10^{10}	11.5×10^{10}	2.5×10^{10}	-5.2	12.7	17	6.46×10^{-9}	5.62×10^{-9}	7500

Table 1: Materials along with the corresponding constitutive coefficients used in this study.

are increased sufficiently. This fact occurs because the present method inherits the characteristic of the finite element method concerning the spatial discretization (namely the mesh dependency of the numerical solution), and it offers a robust alternative method for obtaining the solution of the semi-discretized form. In these Figures, an undershooting or overshooting of results have also been noted at the end of the time span, which is attributed to the non-convergence nature of the method when $t = T$. Various strategies have been introduced in [28] to address this issue, such as solving the problem for $t \in [0, T + \delta T]$ where δT is a small positive number.

The corresponding velocity values are also depicted in Figs. 5 & 6. The analytical results contain a piecewise continuous form with small oscillations in discontinuities. The abrupt changes in the velocity fields create a so-called Gibbs phenomenon in the CFEM results, causing a wavy pattern near the discontinuities and sharp changes. To mitigate the oscillations, one can employ filters to enhance the vanishing rate of time-wise series, smoothening the achieved numerical solutions (see [33]). This filtering scheme is applied at the post-processing stage, and thus, it does not cause an increase in the computational cost. Alternatively, one can use the 'time-step version of the algorithm' (where the total time is divided into several time intervals (see [28]) combined with filters. In Fig. 7, variation of electrical potential has also been calculated and compared to the analytical solution. Similar to the displacement values, the accuracy of the solution for the electrical potential is substantially improved if a more refined mesh with a higher number of time-wise terms is used.

The performance of the new method is further examined by solving case 2 (see Fig. 2). The displacement and velocity values at the mid-point of the bar have been depicted in Figs. 8 & 9. The satisfaction of initial velocity conditions can be seen in Fig. 9 at the onset of the time span, confirming the accuracy of analytical and numerical solutions presented. Also, abrupt changes of the displacement values are observed in Fig. 8, resulting in the jumps of the velocity values shown in Fig. 9. While setting $N = 20$ seems to offer an acceptable solution for displacement values, this is not an appropriate number to capture the velocity field precisely. As mentioned earlier, to overcome the oscillation of the velocity field in the numerical solutions, one can apply the Fourier space filters. In particular, given the Fourier expansion of a periodic function with period 2π:

$$f_N(t) = \sum_{k=-N}^{k=N} \hat{f}_k e^{i\pi t}, \tag{5.5}$$

one can apply a filter function

$$f_N(t) = \sum_{k=-N}^{k=N} \hat{f}_k \beta_f(k/N) e^{i\pi t}, \tag{5.6}$$

where $\beta_f(k/N)$ is a filter function minimizing the effect of higher frequency. The following function is assumed for the filter

$$\beta_f(\eta) = e^{-\alpha\eta^p}, \tag{5.7}$$

in which α and p are fitting parameters. The parameter p should be an even number, and its magnitude is inversely related to the number of time-wise terms(i.e., $p \propto 1/N$). The value of α should also be selected in such a way that the exponential $e^{-\alpha}$ does not exceed machine run-off error (see [33]). In the presented work, the velocity fields are recalculated using the above filter with $p = 2$ and $\alpha = 700$. The filtered results are depicted in Figs. 10 & 11. It can be seen that the use of a filter noticeably smoothens the discontinuous velocity field.

Next, the following error index is defined to quantify the accuracy of the method:

$$E(x) = \sqrt{\frac{\int_0^T (u_R(x,t) - u_N(x,t))^2 dt}{\int_0^T u_R(x,t)^2 dt}}, \tag{5.8}$$

where $u_R(x,t)$ is a reference (analytical) solution and $u_N(x,t)$ is the numerical solution. For different element numbers and time-wise terms, the contours of the error-index have been shown in Figs. 12 & 13, respectively, for cases 1 and 2

at $x = L$. From these figures, it is clear that the error of the approach is reduced when sufficient elements number and time-wise terms are considred. It can be seen for both cases that at least 500 and 800 time-wise terms are required to confine the error below one percent, respectively, for 50 and 100 elements. This fact implies that the desired accuracy of the solutions depends not only on the number of time-wise terms but also on the number of spatial elements. It is also obvious that the error index would be capped if the number of time-wise terms was only increased.

5.2 2d Cases

5.2.1 Free and forced vibration problems

The presented formulation in analyzing 2d dynamic problems associated with piezoelectric materials is investigated through the following examples. A degenerated elastostatic formulation is first implemented, and its results are compared to an existing analytical solution to show the accuracy of the solution procedure in 2d. Also, this problem is used to highlight the difference between stationary and non-stationary responses. The problem is the extension of an elastic prism made of PZT-4h piezoelectric material. The geometry of the problem is shown in Fig. 14, and material parameters have been tabulated in table 1. The following boundary conditions are applied on the edge of the prism:

$$\begin{aligned} &\sigma_{11} = \sigma_{13} = D_1 = 0, \qquad \mathrm{x_1 = \pm a}, \\ &\sigma_{33} = P,\ \sigma_{13} = D_3 = 0, \quad \mathrm{x_3 = \pm h}. \end{aligned} \tag{5.9}$$

The following geometrical parameters are considered: $a = 3m$,$h = 10m$, and $P = 10Pa$. The stationary extension of the piezoelectric prism has been solved analytically by [18], which is used here for comparison (see also [22]). Due to the symmetry, one quadrant of the prism is only simulated. Also, 12×40 uniform quadrilateral elements with linear Lagrange shape functions are used. Some points of interest, denoted by A, B, C, and D in Fig. 14(a), are selected on the prism for quantifying the field variables. The problem is solved using the standard FEM with plane strain condition. A comparison between analytical and numerical solutions was presented in Table 2, where the numbers in parentheses stand for the analytical solution.

An excellent agreement is observed between the two solutions, demonstrating the validity of the numerical calculations

Elastostatic of the 2D problem				
Points	$A(2,0)$	$B(3,0)$	$C(0,5)$	$D(0,10)$
$u_1(\times 10^{-10}m)$	-0.7724 (-0.7722)	-1.0835 (-1.0834)	0.0000 (0.0000)	0.0000 (0.0000)
$u_3(\times 10^{-9}m)$	0.0000 (0.0000)	0.0000 (0.0000)	0.3914 (0.3915)	0.7831 (0.7829)
$\phi(V)$	0.0000 (0.0000)	0.0000 (0.0000)	1.2185 (1.2183)	2.4371 (2.4373)
$\sigma_{11}(\frac{N}{m^2})$	-0.0000 (0.0000)	-0.0000 (0.0000)	0.0000 (0.0000)	0.0000 (0.0000)
$\sigma_{33}(\frac{N}{m^2})$	9.9994 (10.000)	9.9995 (10.000)	9.9997 (10.000)	9.9996 (10.000)
$D_3(\frac{C}{m^2})$	0.0000 (0.0000)	0.0000 (0.0000)	0.0000 (0.0000)	0.0000 (0.0000)

Table 2: The analytical and numerical results for the PZT-4h piezoelectric prism.

in the absence of inertial force.

In the next step, the dynamic behavior of the piezoelectric prism is studied using the new method. For the first analysis, free vibration of a piezoelectric prism subject to initial vertical velocity of $v_3^0 = 10^{-6}\frac{m}{s}$ is solved. The aim here is to demonstrate the accuracy of the numerical formulation in the conservation of energy. Fig. 15 shows the variation of the energy function versus time when different numbers of time-wise terms are used. It can be seen from Fig. 15 that the model can successfully preserve the energy if a sufficient number of time-wise terms is employed. For the case $N = 2000$, the decomposition of total energy to electrical and mechanical energy has been depicted in Fig. 16.

For the next analysis, a forced vibration problem is investigated. The tension is assumed to be applied instantly and remains unchanged during the simulation. A relatively fine mesh with 480 elements (12×40) and $N = 1000$ have been utilized, representing a reference solution for the output generation and the error estimation. The horizontal displacement has been depicted in Fig. 17 for point B. Since the applied load aligns with the vertical direction, a relatively high oscillations is noted for horizontal displacement. Similar to the 1d case, fluctuation at the end of the time span can be attributed to the zero velocity field value at $t = T$, which can be minimized if more time-wise terms are employed. Alternatively, the time-step version of the algorithm can be implemented to reduce the number of time-wise terms required. In this method, the total time interval is divided into smaller time intervals as $T = \frac{\Delta t}{1-\gamma}$, where $0 < \gamma < 1$ is a parameter increasing the length of time span. By using the time-step version of the algorithm with $\gamma = 0.3$, the displacement fields have been recalculated for the case $N = 50$ in the Fig. 18. For comparison, the result corresponding to a single time step with $N = 2000$ are shown in these figures. Clearly, using smaller time-steps (4 steps here), one can precisely derive the original solution corresponding to $N = 2000$ with a lower N. Also, the fluctuation at the end of the

time span has been removed using the time-step version of the algorithm.
In Fig. 19, the velocity profile has been reported for point D. This result shows more oscillations compared to the displacement fields. The filter function is applied ($p = 2$ and $\alpha = 700$) to exclude the excessive oscillations (see Fig. 20). As can be seen, the filter could smoothen the velocity field. Also in Fig. 20, the results of HHT-α method with $\alpha = -0.3$ and $\Delta t = \frac{T}{2000}s$ has been depicted, showing a similar trend to a version of the new approach equipped with filter function. This fact is because the HHT-α method possesses an additional damping parameter, i.e., α, which can exclude the spurious part of the solution. Next, the errors of the method have been determined in terms of the number of elements and N. For points D and B, the error norms have been calculated in Figs. 21(a) & 22(a). As can be seen, the error decreases by the simultaneous increase of the number of elements and N. Also, it is noticed that the number of time-wise terms achieving the cap of error increases if the element number increases. Moreover, the error of lateral displacement is relatively higher than the error of vertical displacement, thanks to the direction of loading. For a similar problem with only transversely isotropic properties for the material, error values for displacement have also been calculated in Figs. 21(b) & 22(b) for points D and B, respectively. Obviously, the convergence speed is increased if the effect of piezoelectricity is excluded from the calculation.
The spatial variation of the field variables has then been computed. Figures 23, 24, & 25 demonstrate the snapshots of the horizontal displacement, vertical displacement, and electrical potential at $t = \frac{T}{16}$, $t = \frac{T}{8}$, $t = \frac{3T}{16}$ and $t = \frac{T}{4}$. Roughly, the higher and lower values of vertical displacement have occurred at these times. By comparing the static solution (Table 2) with the results of the dynamic case, one can observe that the amount of the deformation and electrical potential has become more than twice in the dynamic case due to inertial forces. For the selected times, the deformed shape of the prism has been shown in Fig. 26. Figures 27 & 28 show the velocity field ,respectively, without and with applying the filter. As can be seen, the filter reduces the excessive artificial oscillations.
Finally, as depicted in Fig. 29, a transient electric boundary condition is exerted on the same piezoelectric plate. In this regard, two ends of the plate are connected to opposite transient triangular voltage, as shown in Fig. 29. The resultant velocity profiles due to this excitation have been displayed in Figs.30 & 31 for points B and D, respectively. From these Figures, one can conclude that the phase lag created in lower N's is eliminated by increasing N. Furthermore, the total internal energy function decomposed to the mechanical and electrical components was plotted in Fig. 32 using $N = 2000$ time-wise terms. The energy conversion from the electrical to mechanical is noted after the disappearance of the external voltage, which is the resultant of the inverse piezoelectric effect. Also, the internal energy conservation is maintained once the impulse electrical displacement disappears (i.e., in the free vibration phase).

5.2.2 Wave Characteristics problem

The capability of the proposed method in determining the wave characteristics of piezoelectric materials is considered here. To this end, a piezoelectric plate under impulsive loading is analyzed, and the dispersion curves corresponding to the surface lamb waves are numerically determined. The geometry of the problem is shown in Fig. 33(a), where $a = 100mm$ $h = 0.5mm$. The electrical and mechanical boundaries are restrained in the far-right direction. A discretization consisting of 5000 elements (i.e., 500×10) was considered where the geometry was approximated by elements of the size $l_{ex} = 0.2 \times 10^{-3}$ and $l_{ey} = 0.05 \times 10^{-3}$. According to [34], this size accurately simulates waves with a wavelength of less than $\lambda_{\min} = 20l_e$. A number of impulse point loads are applied on multiple locations of the plate, as shown in Fig. 33(a).
To obtain the dispersion curve, we follow the method mentioned in [34]. In particular, the time history of nodal displacements corresponding to the top face of the plate is recorded. The dispersion curve can then be determined by applying the 2D-FFT function to the aforementioned data, revealing various surface waves aligned with the peaks. In this example, the PZT-4h piezoelectric material with the material parameters given in Table 1 is considered. The only exception is that we assumed $c_{11} = 13.9 \times 10^{10} \frac{N}{m^2}$ to be able to verify the numerical results with the available data in the literature. Figure 34 demonstrates the transformed vertical displacement in frequency-wavelength space calculated by the new method with $N = 3000$. Figure 35 illustrates the pick values of amplitude functions for horizontal displacement, along with semi-analytical solutions reported by [35]. In both figures, non-dimensional quantities kh and $\frac{\omega}{\omega_0}$, with $\omega_0 = \sqrt{c_{44}/\rho}/h$ have been utilized for reporting the data. A good match between the numerical and semi-analytical solutions is noted for a wide range of frequencies and wave numbers. However, it can be seen that a finer mesh is required to capture the results of the semi-analytical dispersion curve for higher wave numbers. Comparing Figs. 34 & 35, one can observe that the pick values occurred in the same locations for both 2D-FFT values of vertical and horizontal displacements. In addition, to demonstrate the convergence, we reported the frequency spectrum in Fig. 36 for various N values where $N = 3000$ is representing the reference solution. It is observable from this figure that the accurate solution can be recovered if sufficient time-wise terms are used.
A similar case has been studied to measure the rate of convergence of the new method (see Fig. 33(b)).The only differences here are a single transient triangular displacement is imposed on the nodal points at the top left of the plate,

and a mesh consisting of 50×5 elements is considered. we define the rate of convergence as follows:

$$C_i^q(N,x_1) = \frac{\left| \int_0^{T^{total}} \left(\left(u_i^{N+1}(x_1,x_3^{top},t)\right)^2 - \left(u_i^{5001}(x_1,x_3^{top},t)\right)^2 \right) dt \right|}{\left| \int_0^{T^{total}} \left(\left(u_i^{N}(x_1,x_3^{top},t)\right)^2 - \left(u_i^{5001}(x_1,x_3^{top},t)\right)^2 \right) dt \right|^q}, i = 1,3, \tag{5.10}$$

where q denotes the order of convergence, $\mathbf{u}^N$ stands for the displacement vector obtained from the new method when N time-wise term is used, and $\mathbf{u}^{5001}$ is the reference solution. we say the method converges at the rate q when $\lim_{N\to\infty} C_i^q(N,x_1)$ converges to a finite value. Here, we consider linear rate of convergence, i.e., when $q = 1$. Also, the upper limit of the above integral is $T^{total} = 40\mu s$, and $x_3^{top} = .5mm$. We employed the trapezoidal rule with 20000 sample points to take the above integrals. The results corresponding to C_1^1 and C_3^1 were shown in Figs. 37 & 38, respectfully. As can be seen from these figures, we have $\lim_{N\to\infty} C_i^q(N,x_1) = 1, 0 \le x_1 \le 0.1, i = 1,3$, implying that the method converged at least at a linear rate.

6 Conclusion

A new dynamic finite element method for elastodynamics problems of linear piezoelectric materials was presented. The coupled governing equations representing the motion of electro-mechanical behavior of piezoelectric material were written in terms of alternative field equations, where the effect of initial conditions was considered implicitly as a forcing term. A weak formulation based on these equations was then established. The spatial discretization was then performed, while time-wise series was introduced for temporal approximation. The critical feature of convolution formulation is that the model yields a block arrowhead matrix for the corresponding algebraic equations, which substantially decreases the computational cost, making it possible to choose an arbitrary number of time-wise terms. Several 1d examples involving piezoelectric materials were solved and compared with available analytical solutions to validate the model. It was observed that the error of the method decreases if both sufficient time-wise terms and the number of elements are employed. Also, the use of filter functions in the post-processing stage can minimize the oscillations of solutions. The performance of the method was further evaluated by solving 2d problems. It was shown that by implementing the time-step version of the algorithms, the fluctuation of the solution can be substantially omitted at the end of the time span. The new dynamic method converges to the solution regardless of the time step length. This fact implies that the approach can be successfully adopted for analyses requiring large time steps. In addition, in contrast to time integration methods, the solution can converge in the whole time interval except at the end of the time interval. As shown through the numerical results, the latter problem can be fully addressed when the time-step version of the algorithm is employed.

A Appendix

Definition 3. *Denote $L^2(0,T;\mathrm{H}^1(V))$ as a Hilbert space with inner product*

$$\int_0^T (u(t),v(t))dt, \tag{A.1}$$

whose elements are in the Hilbert space $\mathrm{H}^1(\mathrm{V})$ for $0 \le t \le T$ and

$$\int_0^T \|u(t)\|^2 dt < \infty. \tag{A.2}$$

Additionally, in (A.1) and (A.2), $(,)$ and $\|\|$ represent the inner product and norm of $\mathrm{H}(V)$, respectively.

Now, we have the following statement:

Lemma 1. [28] *Let ϑ be an element of $L^2(0,T;\mathrm{H}^1(V))$, and the following holds*

$$\int_\Omega \omega(\mathbf{x})dV \int_0^T \vartheta(\mathbf{x},T-\tau)\cos(\frac{j\pi\tau}{T})d\tau = 0, \quad j = 0,...,\infty, \tag{A.3}$$

for every $\omega \in \mathrm{H}^1(V)$. *Then*

$$\vartheta = 0 \qquad on \quad \overline{V} \times [0,T], \tag{A.4}$$

in the sense of

$$\int_V \int_0^T \vartheta^2(\mathbf{x},t)dtdV = 0. \tag{A.5}$$

The statement in Lemma 1 can be written in terms of all weight functions $w \in L^2(0,T;\mathrm{H}^1(\mathrm{V}))$:

Remark 1. [28] *Let* $\vartheta \in L^2(0,T;\mathrm{H}^1(V))$ *such that*

$$\int_V dV \int_0^T \vartheta(\mathbf{x},T-\tau)\, w(\mathbf{x},\tau)d\tau = 0, \tag{A.6}$$

for every $w \in L^2(0,T;\mathrm{H}^1(\mathrm{V}))$. *Then* $\vartheta = 0$ *in the sense of (A.5).*

Remark 2. [28] *A direct consequence of Remark 1:* $\vartheta \in L^2(0,T;\mathrm{H}(V))$ *is zero in the sense of (A.5) if:*

$$\int_V [\vartheta * w](\mathbf{x},t)dV = 0, \quad 0 < t \leq T, \tag{A.7}$$

for every $w \in L^2(0,T;\mathrm{H}(V))$.

It is noticed that, in a similar fashion, the same results hold true for the boundaries ∂V_{σ_i}, $i = 1,2,3$. For example, we have:

Remark 3. [28] $\vartheta \in L^2((0,T) \times \partial V_{\sigma_i})$ *is zero in the sense of (A.5) if:*

$$\int_{\partial V_{\sigma_i}} [\vartheta * w](\mathbf{x},t)dS = 0, \quad 0 < t \leq T, \tag{A.8}$$

for every $w \in L^2((0,T) \times \partial V_{\sigma_i})$.

Remark 4. [28] *Based on (A.3), similar results corresponding to Remarks 2 and 3 hold when (A.7) and (A.8) are, respectively, replaced by:*

$$\int_0^T \int_V \vartheta(\mathbf{x},t)w(\mathbf{x},t)dVdt = 0, \tag{A.9}$$

and

$$\int_0^T \int_{\partial V_{\sigma_i}} \vartheta(\mathbf{x},t)w(\mathbf{x},t)dSdt = 0. \tag{A.10}$$

Thus, conceptually, one can define a weak formulation corresponding to (2.8) where either the classical dot product or convolution product in time is utilized. However, it is noticed that there is no computational difference between these two forms for the space-temporal shape functions used herein.

B Appendix

The analytical results for elastodynamics of a piezoelectric bar are presented in this section. The reduced version of governing equations reads:

$$\begin{aligned} \sigma_{33,3} &= \rho \ddot{u}_3, \\ D_{3,3} &= 0. \end{aligned} \tag{B.1}$$

Also, the constitutive equations are:

$$\begin{aligned} \sigma_{33} &= c_{33}u_{3,3} + e_{33}\varphi_{,3}, \\ D_3 &= e_{33}u_{3,3} - \varepsilon_{33}\varphi_{,3}. \end{aligned} \tag{B.2}$$

The governing equations in terms of displacements and electric potential can be obtained by employing (B.2) in (B.1):

$$\begin{aligned} &c_{33}u_{3,33} + e_{33}\varphi_{,33} = \rho\ddot{u}_3, \\ &e_{33}u_{3,33} - \varepsilon_{33}\varphi_{,33} = 0. \end{aligned} \tag{B.3}$$

The equation $(B.3)_2$ implies:

$$\varphi = \frac{e_{33}}{\varepsilon_{33}}u_3 + B_1 x_3 + B_2 \tag{B.4}$$

Substituting the second derivative of (B.4) into the equation$(B.3)_1$, one can write:

$$\bar{c}_{33}u_{3,33} = \rho\ddot{u}_3, \tag{B.5}$$

with $\bar{c}_{33} = \left(c_{33} + \frac{{e_{33}}^2}{\varepsilon_{33}}\right)$. Next, $(5.2)_1$ implies $B_2 = V_1$. Considering (5.2), $(5.3)_1$, (B.2), and (B.4), we then find B_1 for the first and second cases, respectively:

$$\begin{aligned} B_1 &= \frac{-e_{33}}{\varepsilon_{33}L}u_3(L,t) + \frac{V_2 - V_1}{L}, \\ B_1 &= \frac{-\hat{d}_3}{\varepsilon_{33}}. \end{aligned} \tag{B.6}$$

The electrical boundary conditions at $x = L$ can be expressed in terms of displacements if $(B.6)_1$ and $(B.6)_2$ are substituted into $(B.4)$, and the equation $(B.2)_1$ is used. The equivalent displacement boundary conditions at $x = L$ can then be written for the first and second cases, respectively:

$$\begin{aligned} &\bar{c}_{33}u_{3,3}(L,t) - \left(\frac{\bar{c}_{33} - c_{33}}{L}\right)u_3(L,t) = \hat{\sigma}_{33} - \frac{e_{33}}{L}\left(V_2 - V_1\right), \\ &\bar{c}_{33}u_{3,3}(L,t) = \hat{\sigma}_{33} + \frac{e_{33}\hat{d}_3}{\varepsilon_{33}}. \end{aligned} \tag{B.7}$$

To use the method of separation of variables, a homogeneous boundary condition is developed. To this end, the following form for displacement is considered:

$$u_3(x_3,t) = \tilde{u}_3(x_3,t) + A' x_3. \tag{B.8}$$

Where $\tilde{u}_3$ is auxiliary function satisfying the homogeneous boundary conditions:

$$\begin{aligned} &\bar{c}_{33}\tilde{u}_{3,3}(L,t) - \left(\frac{\bar{c}_{33} - c_{33}}{L}\right)\tilde{u}_3(L,t) = 0, \\ &\tilde{u}_{3,3}(L,t) = 0. \end{aligned} \tag{B.9}$$

As a result, A' can be obtained as:

$$\begin{aligned} A' &= \frac{\hat{\sigma}_{33} - \frac{e_{33}}{L}\left(V_2 - V_1\right)}{c_{33}}, \\ A' &= \frac{\hat{\sigma}_{33} + \frac{e_{33}\hat{d}_3}{\varepsilon_{33}}}{\bar{c}_{33}}. \end{aligned} \tag{B.10}$$

Therefore the governing equation in a transformed domain can be written as

$$\bar{c}_{33}\tilde{u}_{3,33} = \rho\ddot{\tilde{u}}_3, \tag{B.11}$$

which is subjected to the boundary conditions $\tilde{u}_3(0,t) = 0$, $(B.9)_1$, and $(B.9)_2$. The separation of variables method is then adopted to find the general solution of $(B.11)$ and $(B.8)$, which gives:

$$u_3(x_3,t) = A' x_3 + \sum_{i=1}^{\infty}\left(A_i \sin\left(\lambda_i t\sqrt{\bar{c}_{33}/\rho}\right) + B_i \cos\left(\lambda_i t\sqrt{\bar{c}_{33}/\rho}\right)\right)\sin\left(\lambda_i x_3\right), \tag{B.12}$$

where λ_i's are determined from the characteristic equations for the first and second cases, respectively:

$$\begin{aligned} &\bar{c}_{33}\lambda_i + \left(\frac{\bar{c}_{33} - c_{33}}{L}\right)\tan\left(\lambda_i L\right) = 0, \\ &\cos\left(\lambda_i L\right) = 0. \end{aligned} \tag{B.13}$$

Finally, A_i's and B_i's can be obtained by imposing initial conditions(e.g., $\tilde{u}_3(x_3,0) = u_3^0 - A' x_3$, $\dot{\tilde{u}}_3(x_3,0) = v_3^0$):

$$\begin{aligned} A_i &= \frac{2}{L(\lambda_i\sqrt{\bar{c}_{33}/\rho})}\int_0^L \sin\left(\lambda_i x_3\right) v_3^0 dx_3, \\ B_i &= \frac{2}{L}\int_0^L \sin\left(\lambda_i x_3\right)\left(u_3^0 - A' x_3\right) dx_3. \end{aligned} \tag{B.14}$$

References

[1] J. Y. Li, "Uniqueness and reciprocity theorems for linear thermo-electro-magneto-elasticity," *Q. J. Mech. Appl. Math.*, vol. 56, no. 1, pp. 35–43, 2003.

[2] C. Miehe, D. Rosato, and B. Kiefer, "Variational principles in dissipative electro-magneto-mechanics: A framework for the macro-modeling of functional materials," *Int. J. Numer. Meth. Eng.*, vol. 86, no. 10, pp. 1225–1276, 2011.

[3] R. Li and G. A. Kardomateas, "The mode iii interface crack in piezo-electro-magneto-elastic dissimilar bimaterials," *J. Appl. Mech.*, vol. 73, no. 2, pp. 220–227, 2006.

[4] E. A. Guggenheim, "The thermodynamics of magnetization," *Proc. R. Soc. A*, vol. 155, no. 884, pp. 70–101, 1936.

[5] E. A. Guggenheim, "On magnetic and electrostatic energy," *Proc. R. Soc. A*, vol. 155, no. 884, pp. 49–70, 1936.

[6] P. L. Penfield J. R., L. J. Chu, and H. A. Haus, "Electrodynamics of moving media," tech. rep., Research Laboratory of Electronics (RLE) at the Massachusetts Institute of Technology, 1963.

[7] W. F. Brown, *Magnetoelastic Interactions*. Springer, 1966.

[8] B. D. Coleman and E. H. Dill, "Thermodynamic restrictions on the constitutive equations of electromagnetic theory," *Z. Angew. Math. Phys.*, vol. 22, no. 4, pp. 691–702, 1971.

[9] H. F. Tiersten and C. F. Tsai, "On the interaction of the electromagnetic field with heat conducting deformable insulators," *J. Math. Phys.*, vol. 13, pp. 361–378, mar 1972.

[10] R. D. Mindlin, "Elasticity, piezoelectricity and crystal lattice dynamics," *J. Elast.*, vol. 2, no. 4, pp. 217–282, 1972.

[11] D. F. Nelson, *Electric, Optic, and Acoustic Interactions in Dielectrics*. John Wiley & Sons, 1979.

[12] G. A. Maugin, *Continuum Mechanics of Electromagnetic Solids*, vol. 33. Elsevier, 1988.

[13] A. C. Eringen and G. A. Maugin, *Electrodynamics of Continua I: Foundations and Solid Media*. Springer-Verlag, NY, 1990.

[14] L. D. Landau, J. S. Bell, M. J. Kearsley, L. P. Pitaevskii, E. M. Lifshitz, and J. B. Sykes, *Electrodynamics of Continuous Media*, vol. 8. elsevier, 2013.

[15] H. Allik and T. J. R. Hughes, "Finite element method for piezoelectric vibration," *Int. J. Numer. Methods Eng.*, vol. 2, no. 2, pp. 151–157, 1970.

[16] R. Lerch, "Simulation of piezoelectric devices by two-and three-dimensional finite elements," *IEEE Trans. Ultrason.*, vol. 37, no. 3, pp. 233–247, 1990.

[17] J. Kim, V. V. Varadan, and V. K. Varadan, "Finite element modelling of structures including piezoelectric active devices," *Int. J. Numer. Methods Eng.*, vol. 40, no. 5, pp. 817–832, 1997.

[18] D. Haojiang, W. Guoqing, and C. Weiqiu, "A boundary integral formulation and 2d fundamental solutions for piezoelectric media," *Comput. Methods Appl. Mech. Eng.*, vol. 158, no. 1-2, pp. 65–80, 1998.

[19] C. M. Landis, "A new finite-element formulation for electromechanical boundary value problems," *Int. J. Numer. Methods Eng.*, vol. 55, no. 5, pp. 613–628, 2002.

[20] Q.-H. Qin, "Variational formulations for tfem of piezoelectricity," *Int. J. Solids Struct.*, vol. 40, no. 23, pp. 6335–6346, 2003.

[21] Q.-H. Qin, "Solving anti-plane problems of piezoelectric materials by the trefftz finite element approach," *Comput. Mech.*, vol. 31, no. 6, pp. 461–468, 2003.

[22] C. Cao, A. Yu, and Q.-H. Qin, "A new hybrid finite element approach for plane piezoelectricity with defects," *Acta Mech.*, vol. 224, no. 1, pp. 41–61, 2013.

[23] J.-F. Deü, W. Larbi, and R. Ohayon, "Piezoelectric structural acoustic problems: Symmetric variational formulations and finite element results," *Comput. Methods Appl. Mech. Eng.*, vol. 197, no. 19-20, pp. 1715–1724, 2008.

[24] D. Legner, J. Wackerfuß, S. Klinkel, and W. Wagner, "An advanced finite element formulation for piezoelectric beam structures," *Comput. Mech.*, vol. 52, no. 6, pp. 1331–1349, 2013.

[25] D. Legner, S. Klinkel, and W. Wagner, "An advanced finite element formulation for piezoelectric shell structures," *Int. J. Numer. Methods. Eng.*, vol. 95, no. 11, pp. 901–927, 2013.

[26] T. Q. Bui, "Extended isogeometric dynamic and static fracture analysis for cracks in piezoelectric materials using nurbs," *Comput. Methods Appl. Mech. Eng.*, vol. 295, pp. 470–509, 2015.

[27] M. E. Gurtin, "Variational principles for linear elastodynamics," *Arch. Rational Mech. Anal.*, vol. 16, no. 1, pp. 34–50, 1964.

[28] A. Amiri-Hezaveh, A. Masud, and M. Ostoja-Starzewski, "Convolution finite element method: an alternative approach for time integration and time-marching algorithms," *Comput. Mech.*, pp. 1–30, 2021.

[29] A. Amiri-Hezaveh, P. Karimi, and M. Ostoja-Starzewski, "Ibvp for electromagneto-elastic materials: variational approach," *Math. Mech. Complex Syst.*, vol. 8, no. 1, pp. 47–67, 2020.

[30] A. Amiri-Hezaveh and M. Ostoja-Starzewski, "A convolutional-iterative solver for nonlinear dynamical systems," *Appl. Math. Lett.*, vol. 130, p. 107990, 2022.

[31] S. Wang, "A finite element model for the static and dynamic analysis of a piezoelectric bimorph," *Int. J. Solids Struct.*, vol. 41, no. 15, pp. 4075–4096, 2004.

[32] T. J. R. Hughes, *The Finite Element Method: Linear Static and Dynamic Finite Element Analysis*. Courier Corporation, 2012.

[33] D. Gottlieb and C.-W. Shu, "On the gibbs phenomenon and its resolution," *SIAM Rev. Soc. Ind. Appl. Math.*, vol. 39, no. 4, pp. 644–668, 1997.

[34] F. Moser, L. J. Jacobs, and J. Qu, "Modeling elastic wave propagation in waveguides with the finite element method," *Ndt & E International*, vol. 32, no. 4, pp. 225–234, 1999.

[35] D. H. Cortes, S. K. Datta, and O. M. Mukdadi, "Dispersion of elastic guided waves in piezoelectric infinite plates with inversion layers," *Int. J. Solids Struct.*, vol. 45, no. 18-19, pp. 5088–5102, 2008.

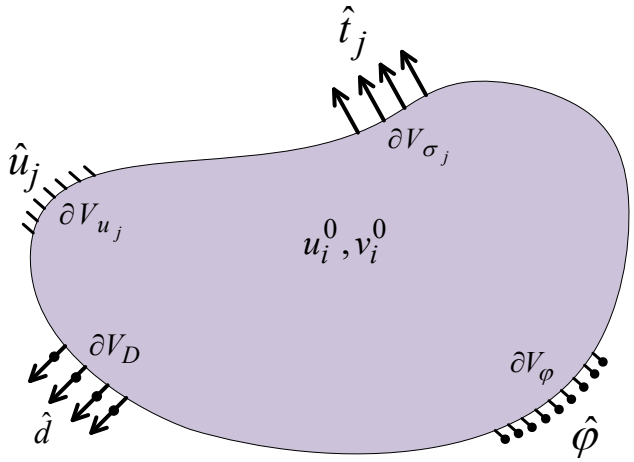

Figure 1: A piezoelectric material subjected to applied electromechanical loading and initial conditions.

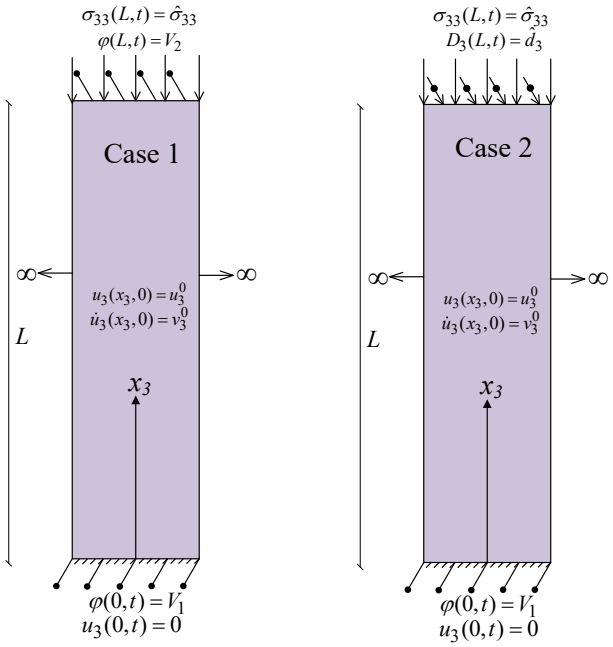

Figure 2: Schematic represtation of 1d problem.

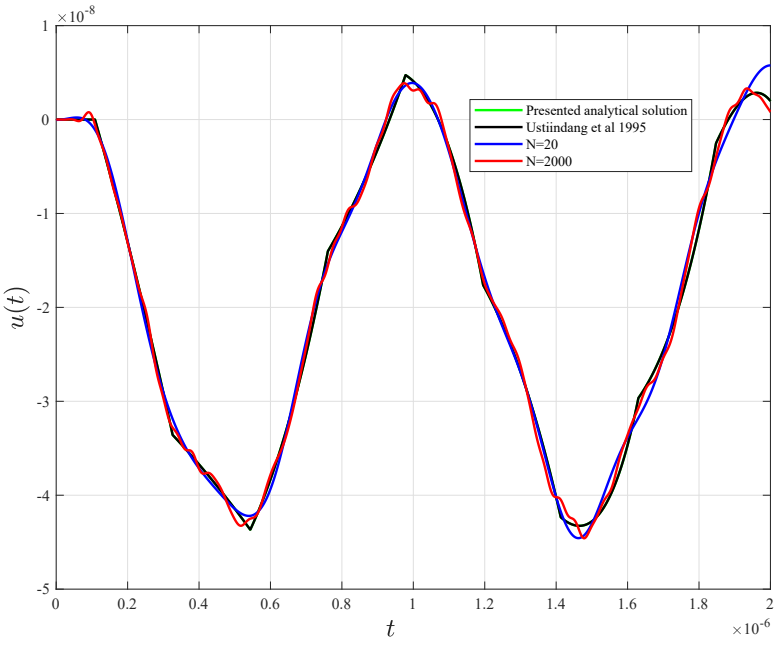

Figure 3: Comparison between analytical and numerical values for the displacement at $x = \frac{L}{2}$ using 10 elements.

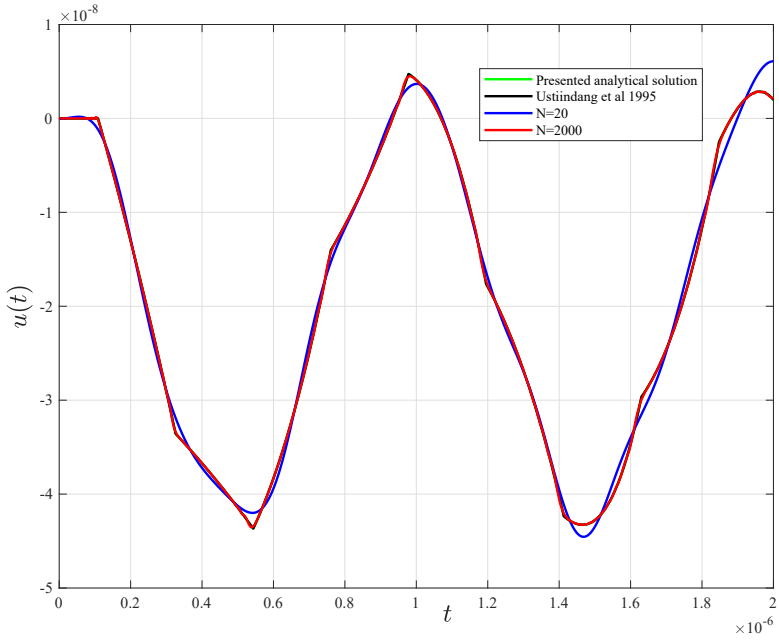

Figure 4: Comparison between analytical and numerical values for the displacement at $x = \frac{L}{2}$ using 100 elements.

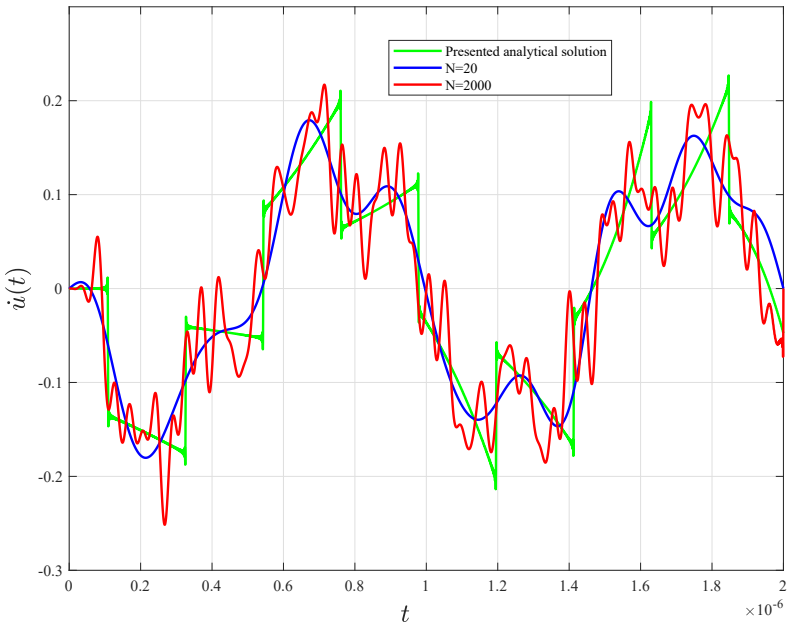

Figure 5: Comparison between analytical and numerical values for the velocity at $x = \frac{L}{2}$ using 10 elements (case 1).

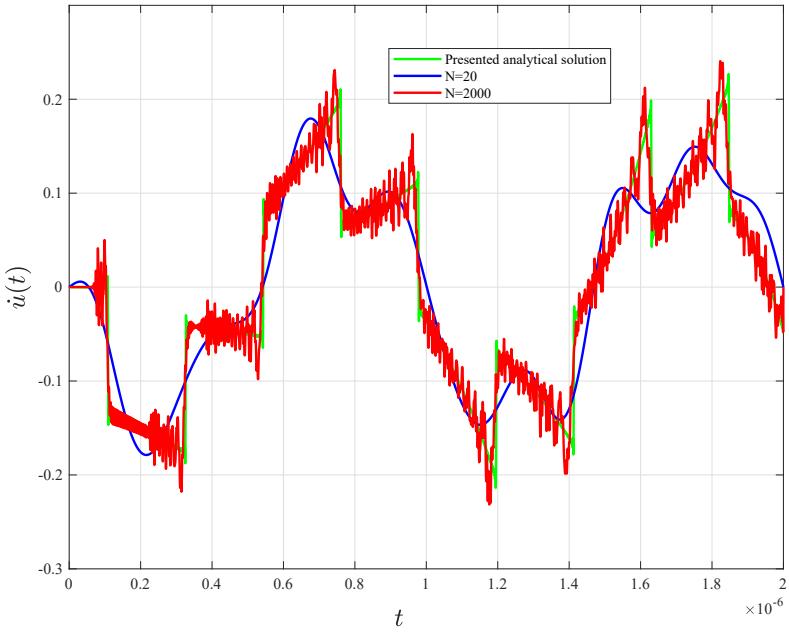

Figure 6: Comparison between analytical and numerical values for the velocity at $x = \frac{L}{2}$ using 100 elements (case 1).

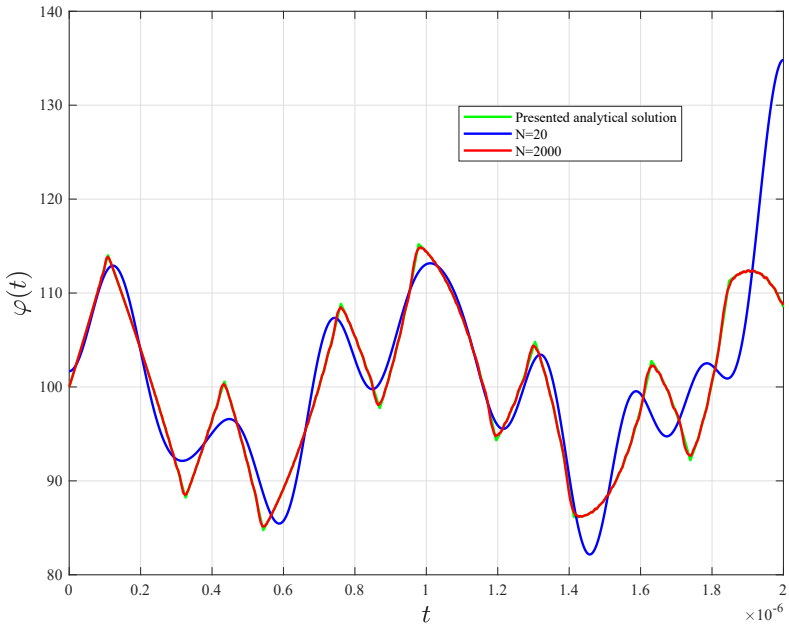

Figure 7: Comparison between analytical and numerical values for the electric potential at $x = \frac{L}{2}$ using 100 elements (case 1).

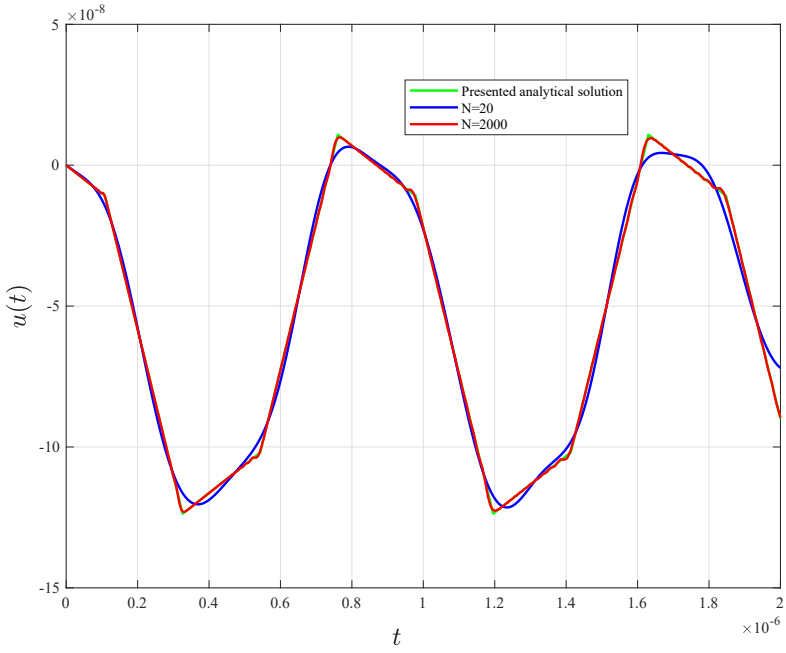

Figure 8: Comparison between analytical and numerical values for the displacement at $x = \frac{L}{2}$ using 100 elements (case 2).

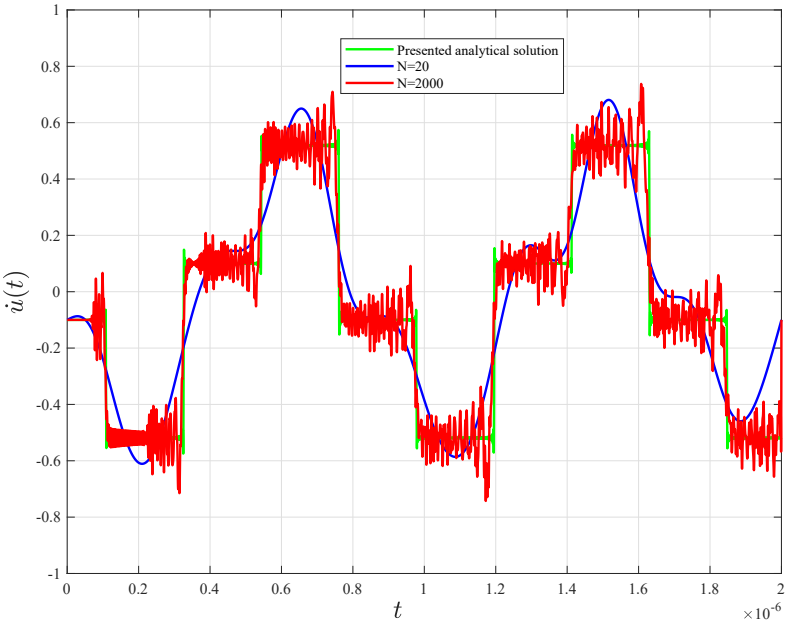

Figure 9: Comparison between analytical and numerical values for the velocity at $x = \frac{L}{2}$ using 10 elements (case 2).

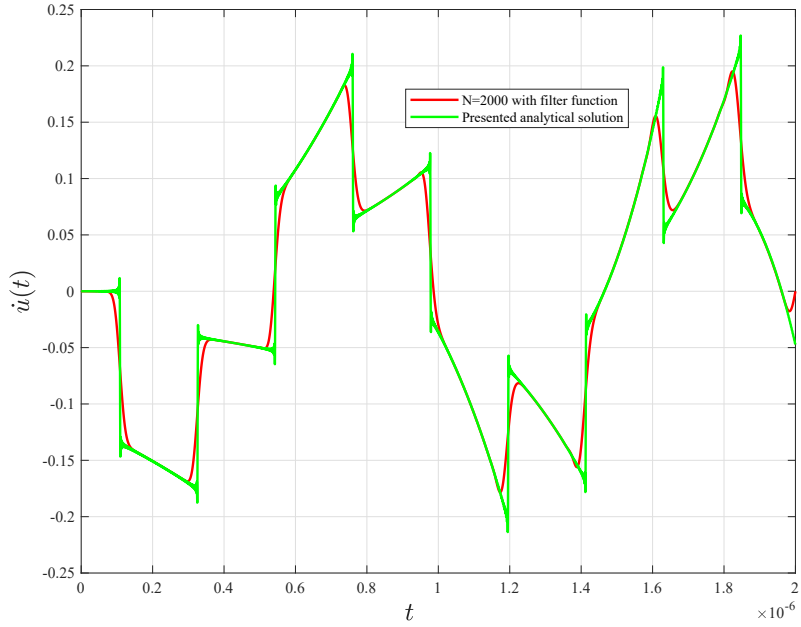

Figure 10: The velocity field at $x = \frac{L}{2}$ after employment of a filter for case 1.

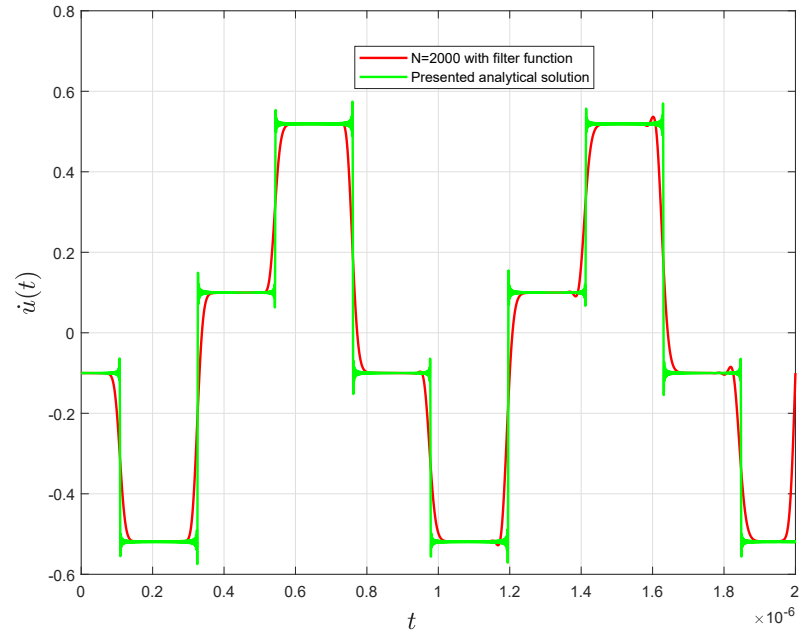

Figure 11: The velocity field at $x = \frac{L}{2}$ after employment of a filter for case 2.

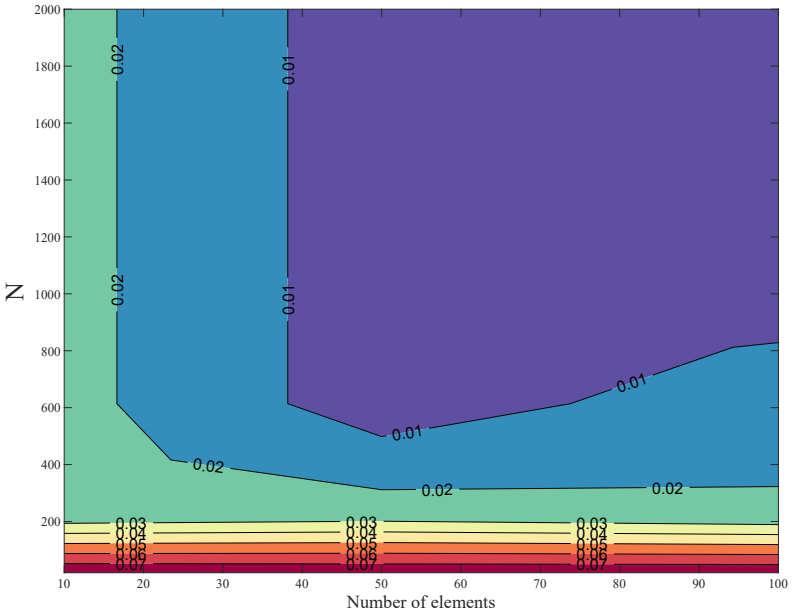

Figure 12: The error norm at $x = L$ based on number of elements and time-wise terms (case 1).

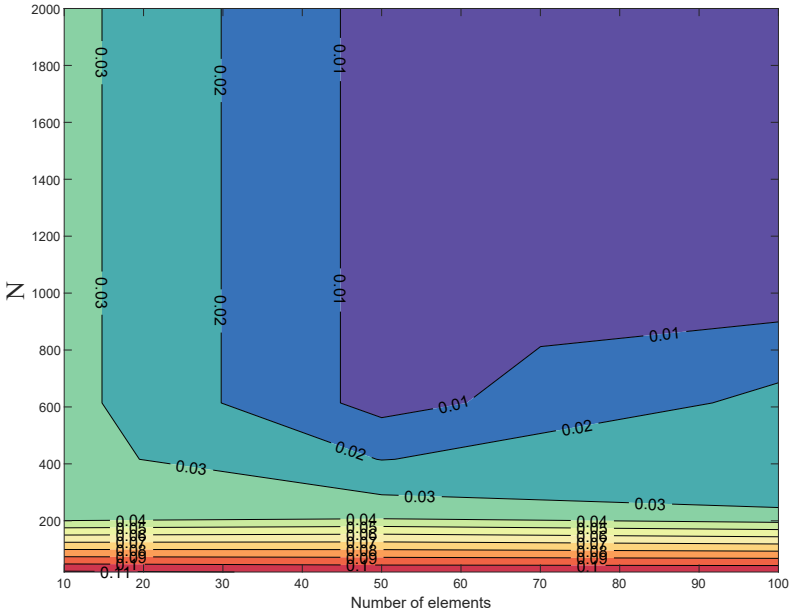

Figure 13: The error norm at $x = L$ based on number of elements and time-wise terms (case 2).

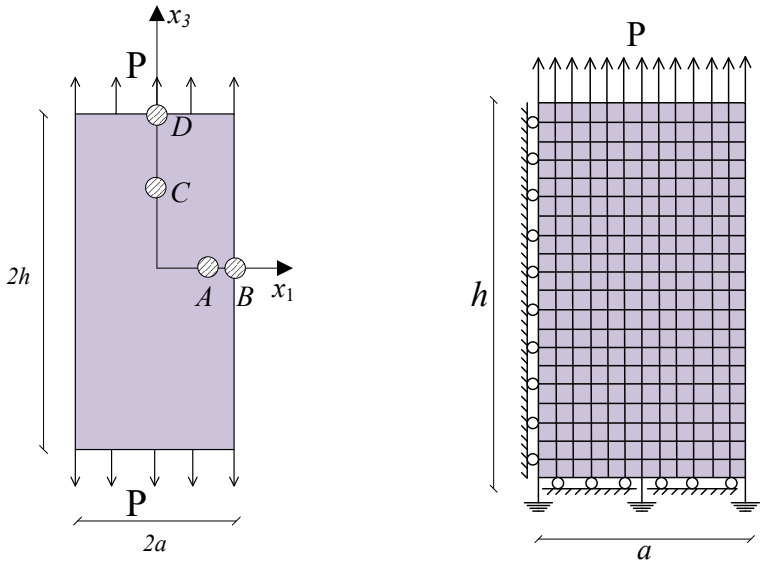

(a) (b)

Figure 14: A piezoelectric prism under tension (a) the geometry (b) discretized configuration.

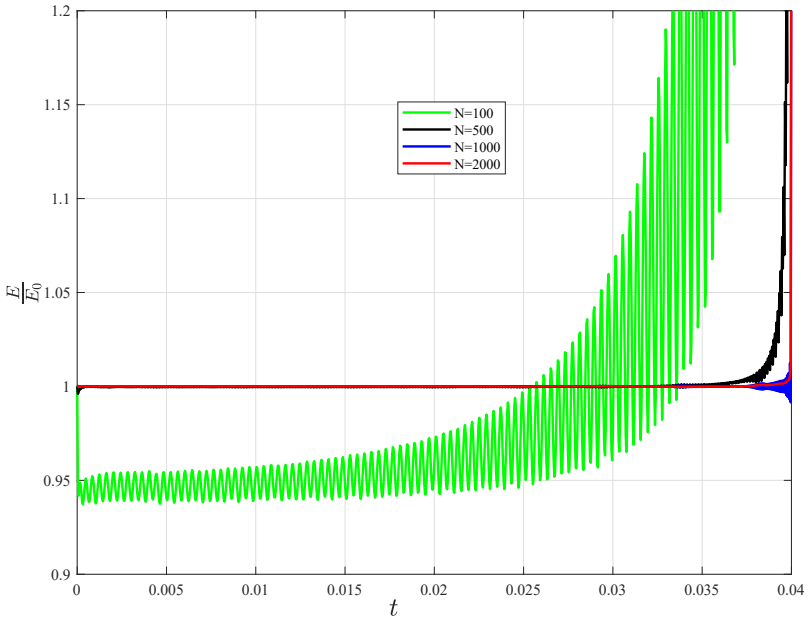

Figure 15: Energy function with respect to time (effect of N).

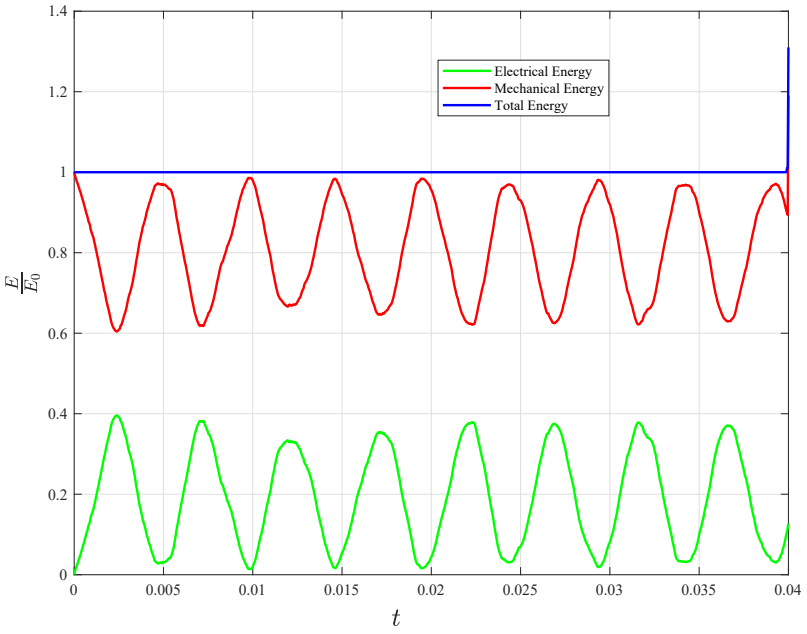

Figure 16: Energy function with respect to time (contribution of electrical and mechanical energy for $N = 2000$).

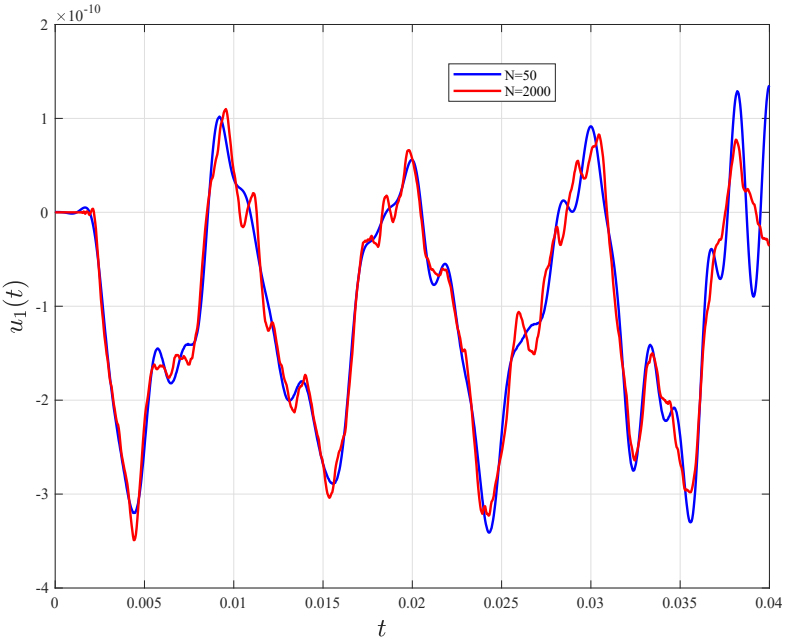

Figure 17: The time variation of the horizontal displacement at point B.

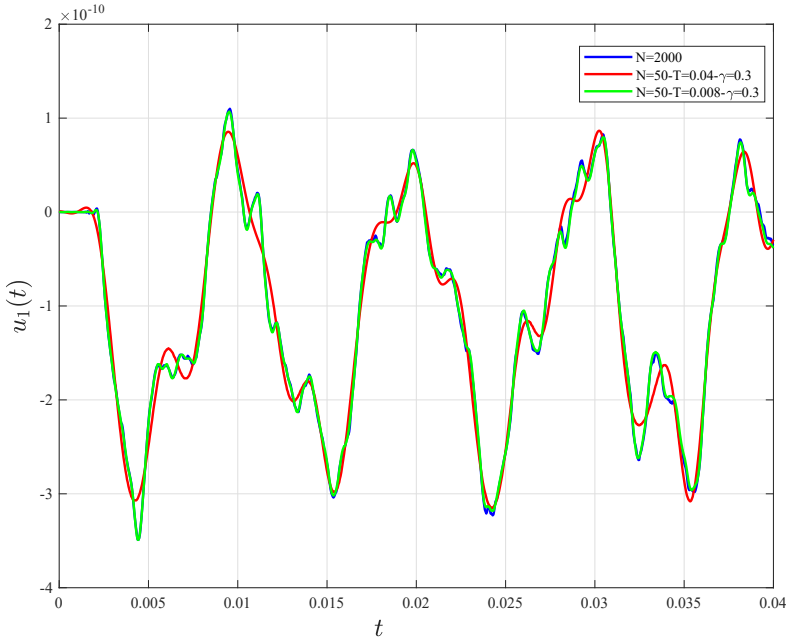

Figure 18: The displacement field obtained with time-step version of algorithm for point B.

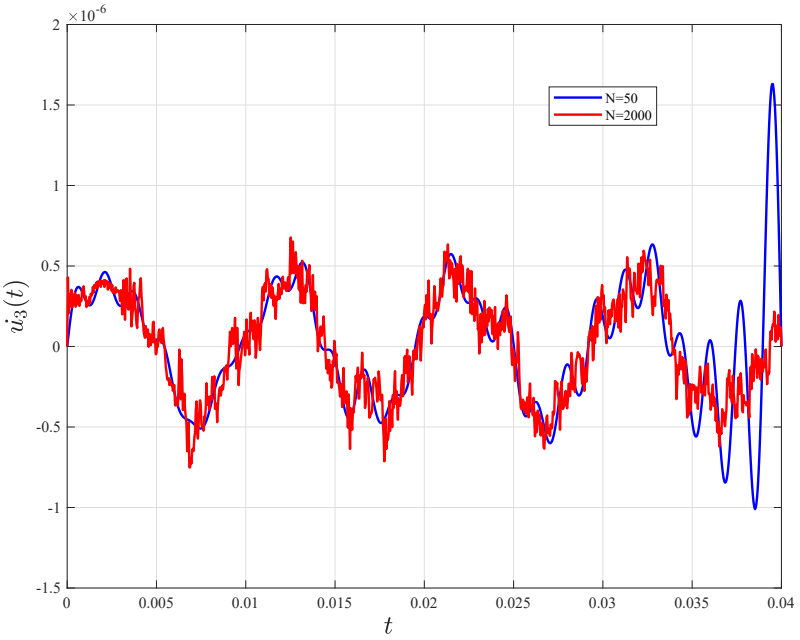

Figure 19: The time variation of the vertical velocity at point D.

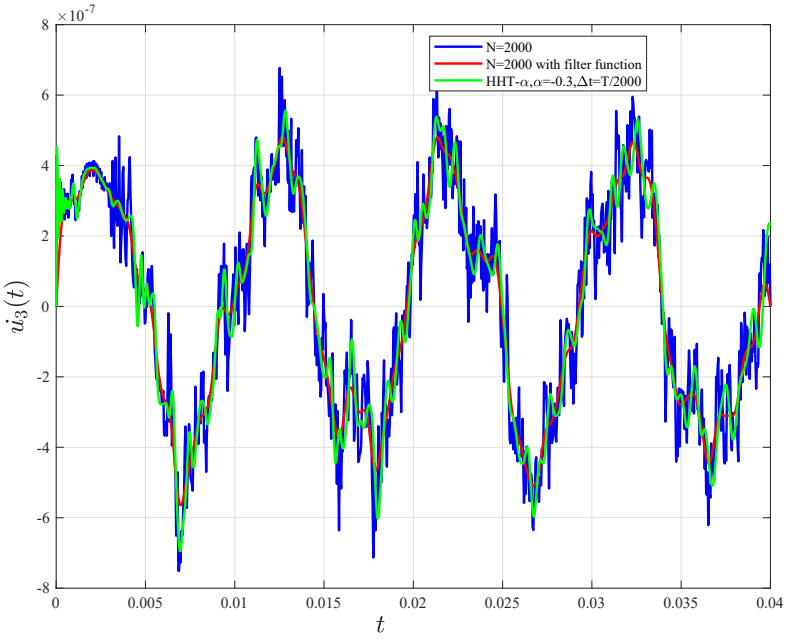

Figure 20: The velocity field with/without a filter for point D.

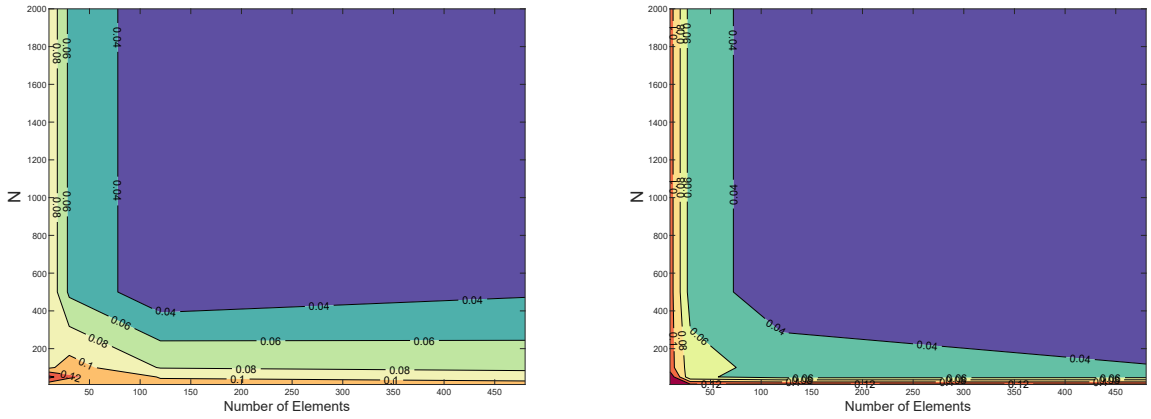

(a) (b)

Figure 21: The error norm of the vertical displacement at point D in terms of number of elements and time-wise terms: (a) for a piezoelectric prism (b) for a transversely isotropic prism.

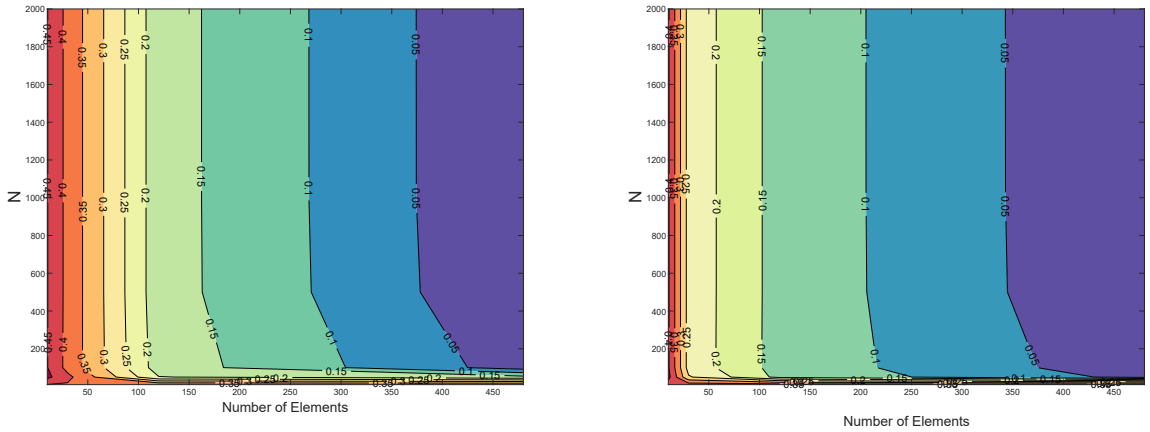

(a) (b)

Figure 22: The error norm of the horizontal displacement at point B in terms of number of elements and time-wise terms (a) for a piezoelectric prism (b) for a transversely isotropic prism.

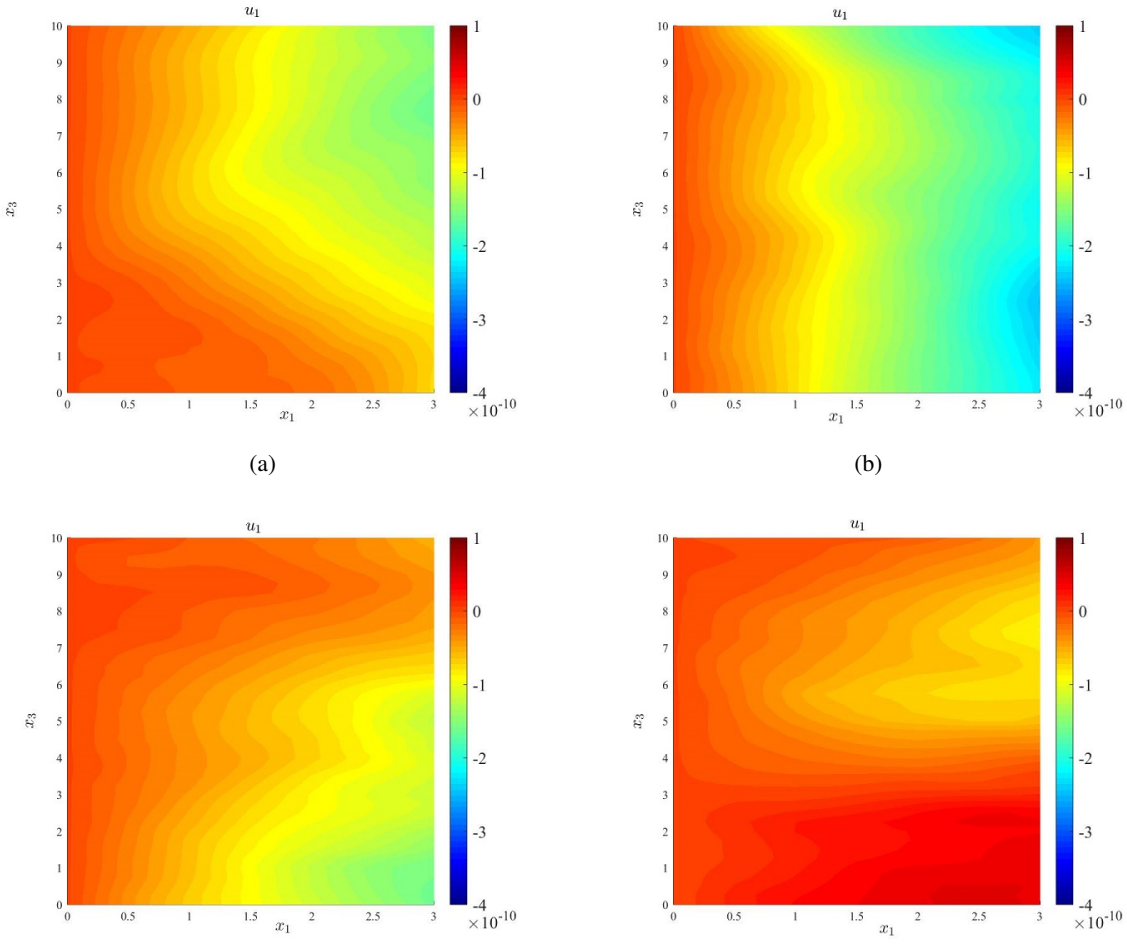

(a) (b)

(c) (d)

Figure 23: Snapshots of u_1 for the piezoelectric material: (a) $t = \frac{T}{16}$ (b) $t = \frac{T}{8}$ (c) $t = \frac{3T}{16}$ (d) $t = \frac{T}{4}$.

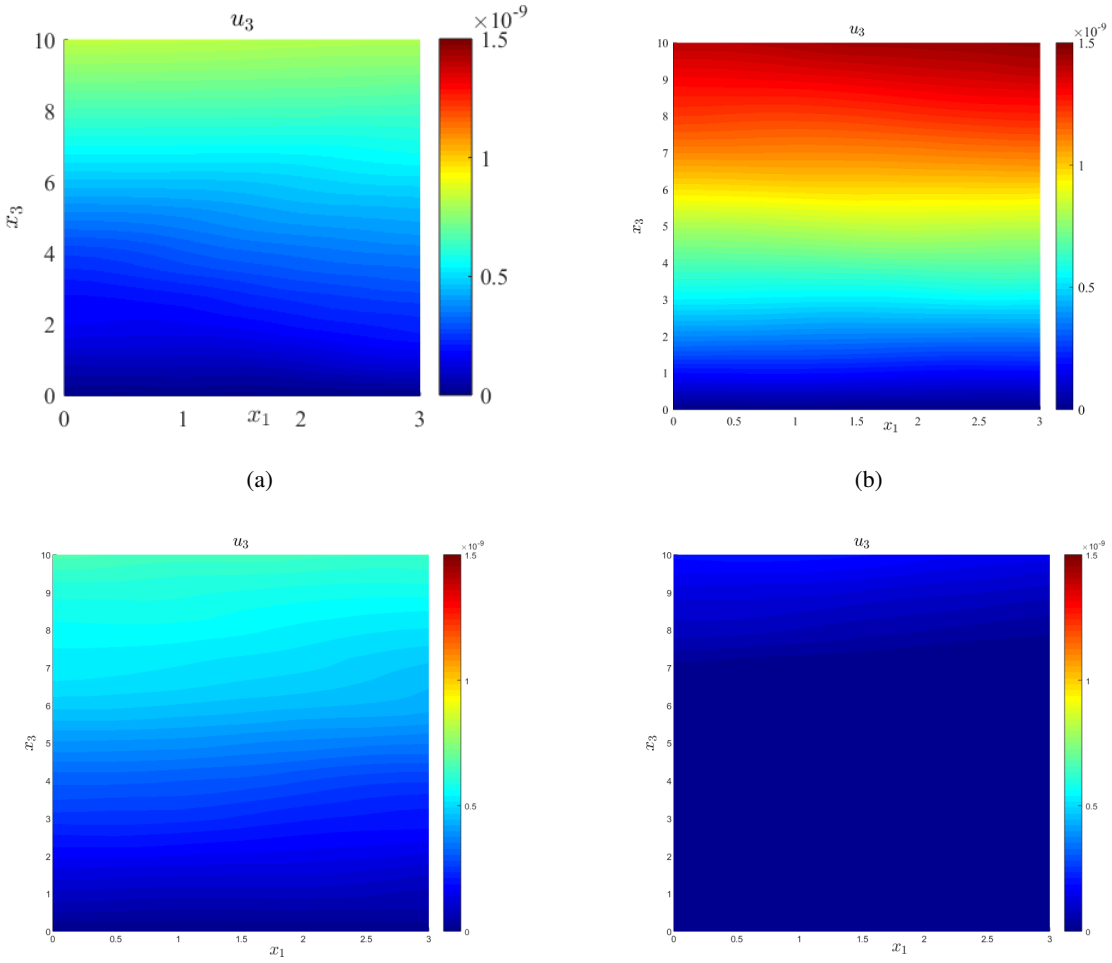

Figure 24: Snapshots of u_3 for the piezoelectric material: (a) $t = \frac{T}{16}$ (b) $t = \frac{T}{8}$ (c) $t = \frac{3T}{16}$ (d) $t = \frac{T}{4}$.

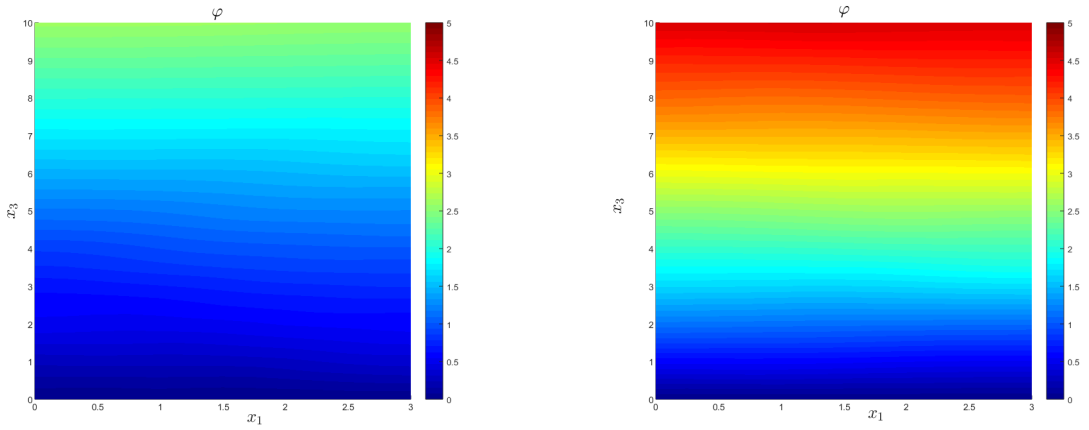

(a) (b)

(c) (d)

Figure 25: Snapshots of ϕ for the piezoelectric material.: (a) $t = \frac{T}{16}$ (b) $t = \frac{T}{8}$ (c) $t = \frac{3T}{16}$ (d) $t = \frac{T}{4}$.

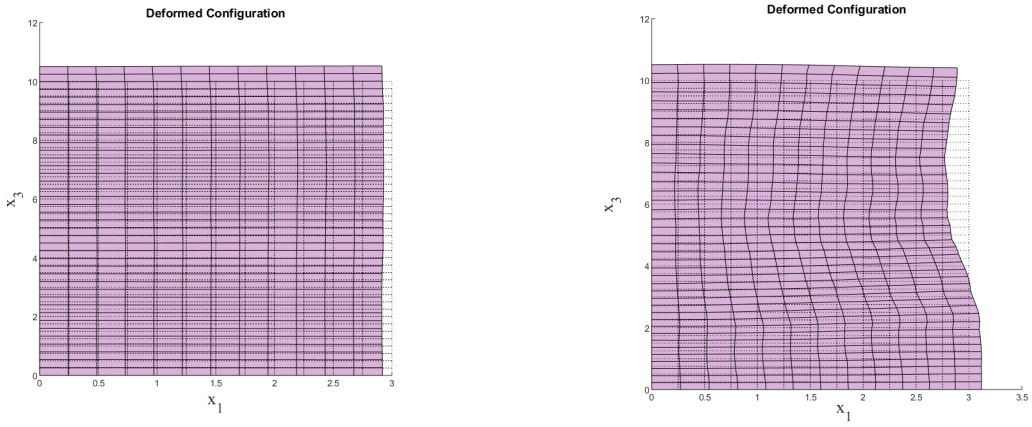

(a) (b)

Figure 26: The deformed shape of the piezoelectric material: (a) $t = \frac{T}{8}$m (b) $t = \frac{T}{4}$.

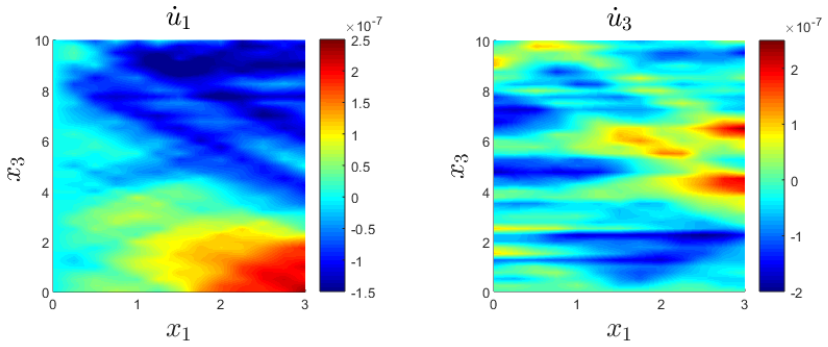

Figure 27: The velocity filed at $t = \frac{T}{8}$.

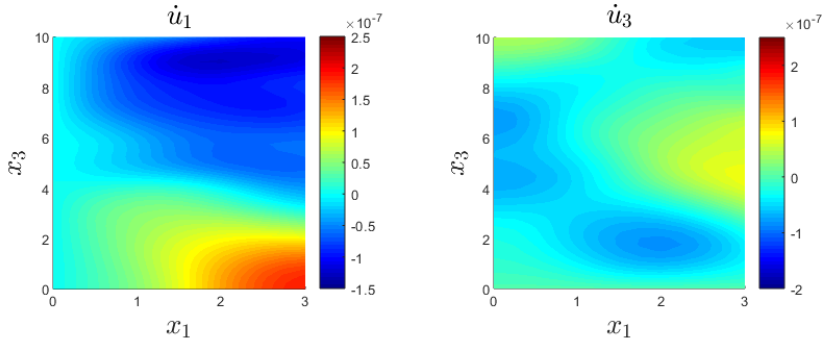

Figure 28: The velocity filed at $t = \frac{T}{8}$ with using filter.

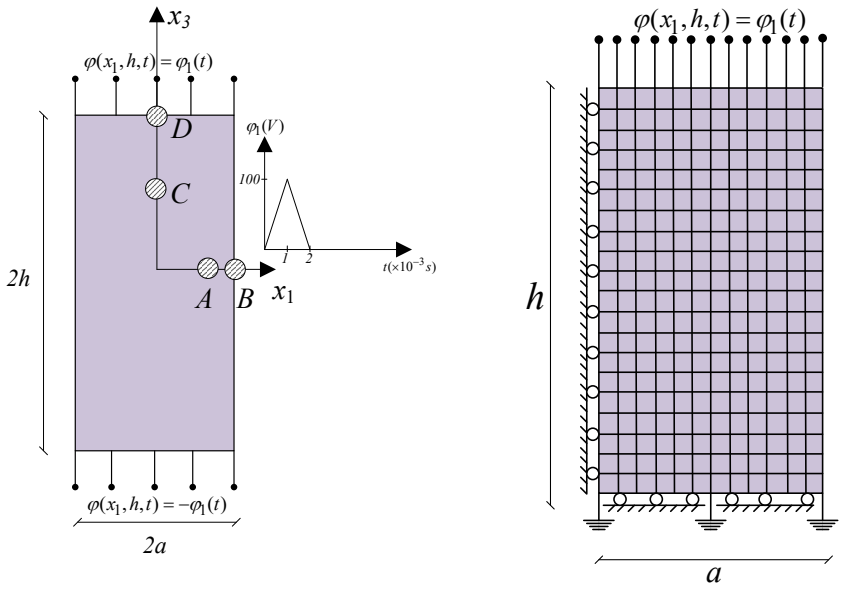

(a) (b)

Figure 29: The beam under multiple impulse displacements (a) the geometry (b) discretized configuration.

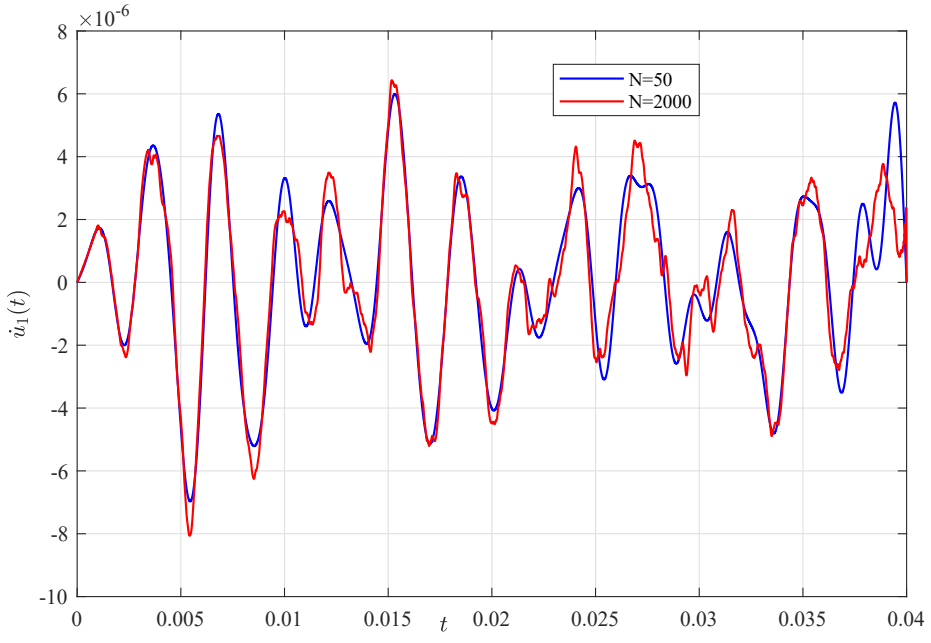

Figure 30: Horizontal velocity profile in piezoelectric plate due to transient electric voltage at point B.

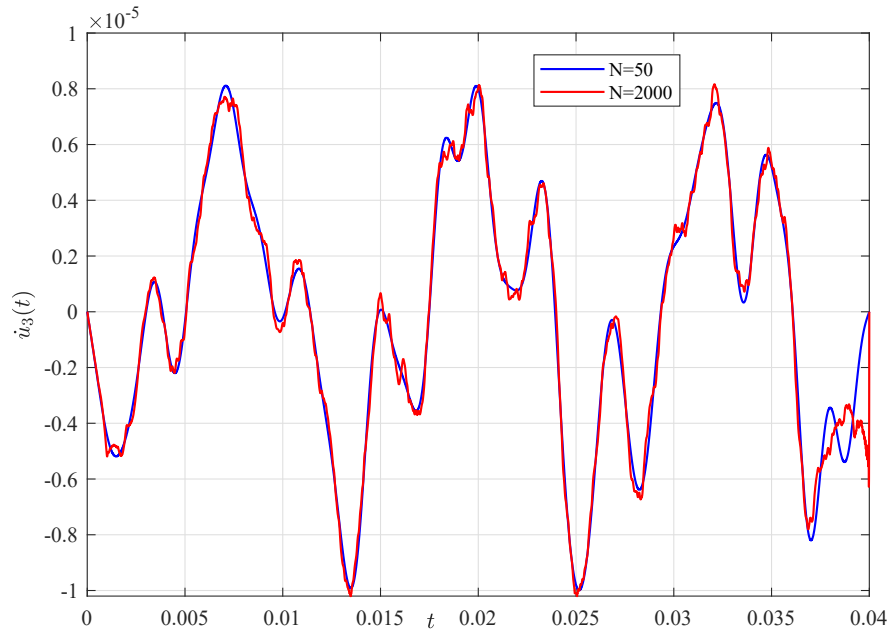

Figure 31: Vertical velocity profile in piezoelectric plate due to transient electric voltage at point D.

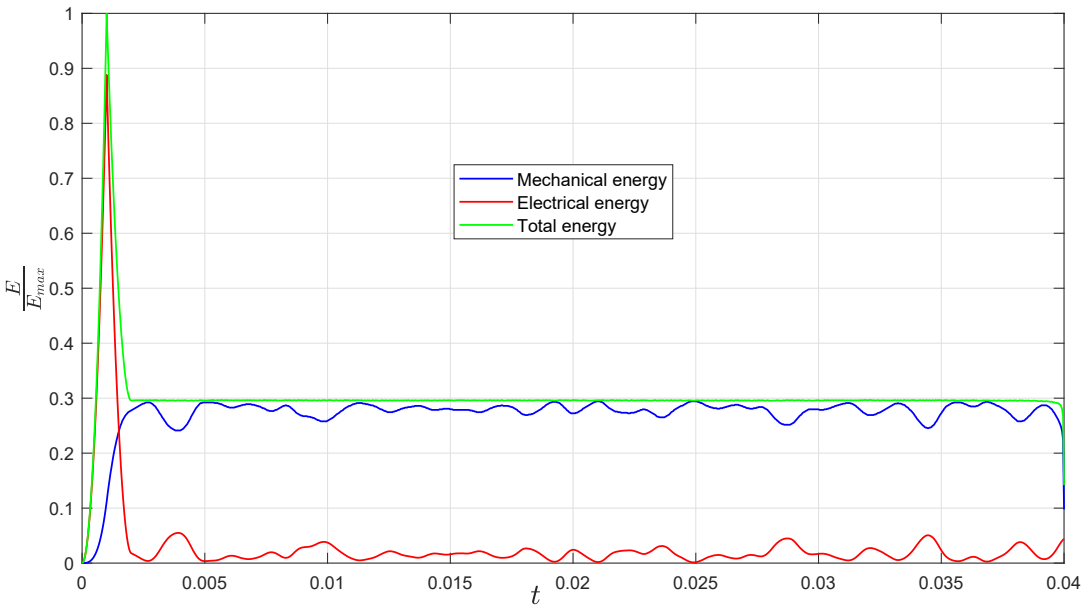

Figure 32: Variation of mechanical, electrical and total energies in piezoelectric plate due to transient electric voltage.

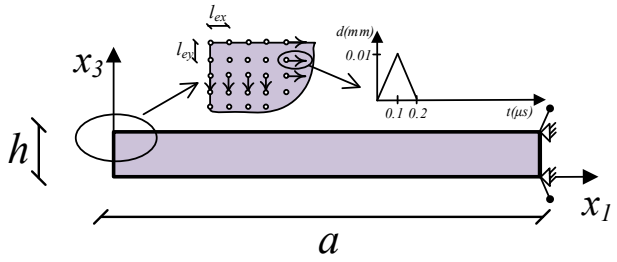

(a)

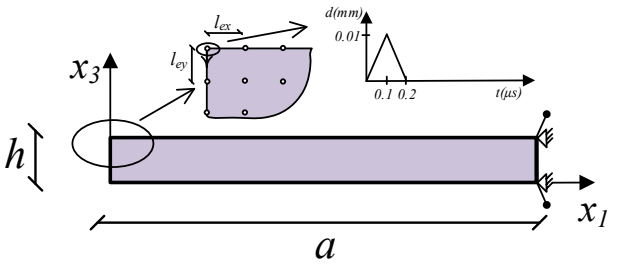

(b)

Figure 33: The geometry of the beam under impulse displacement.

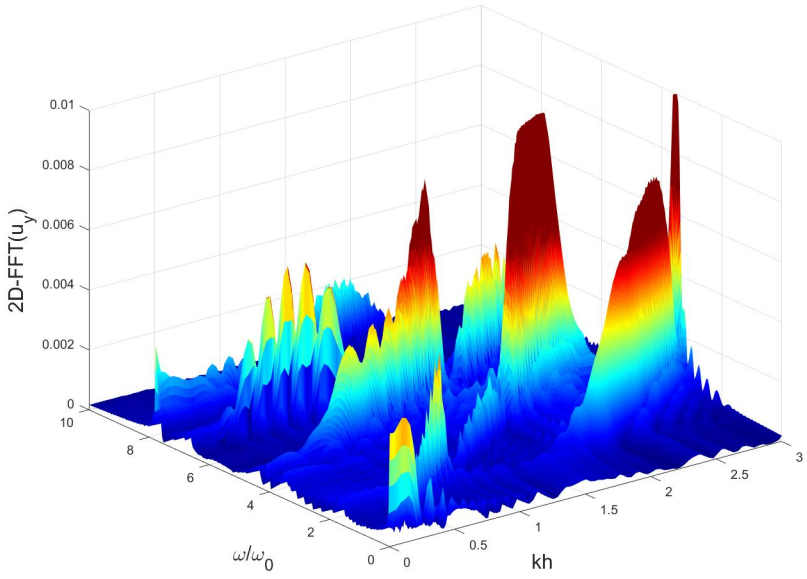

Figure 34: Appearance of dispersion curves in the transformed domain (vertical displacement).

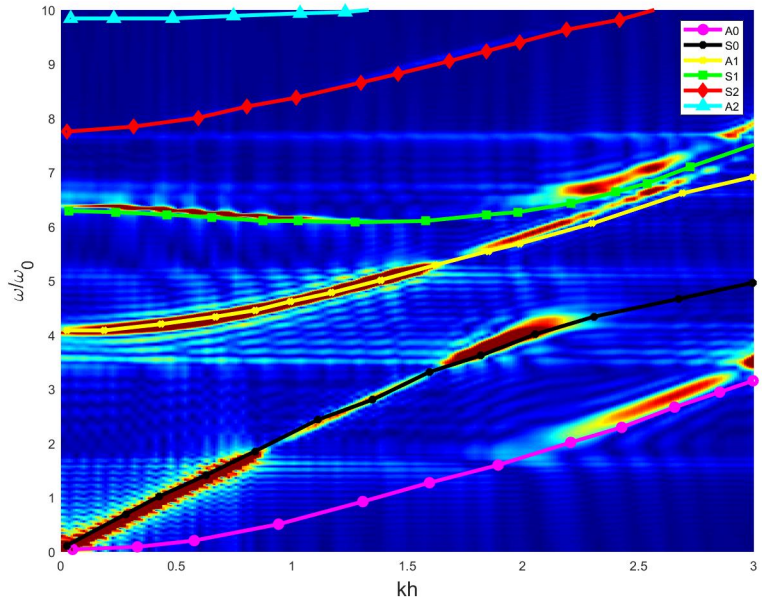

Figure 35: Appearance of dispersion curves in the transformed domain (horizontal displacement).

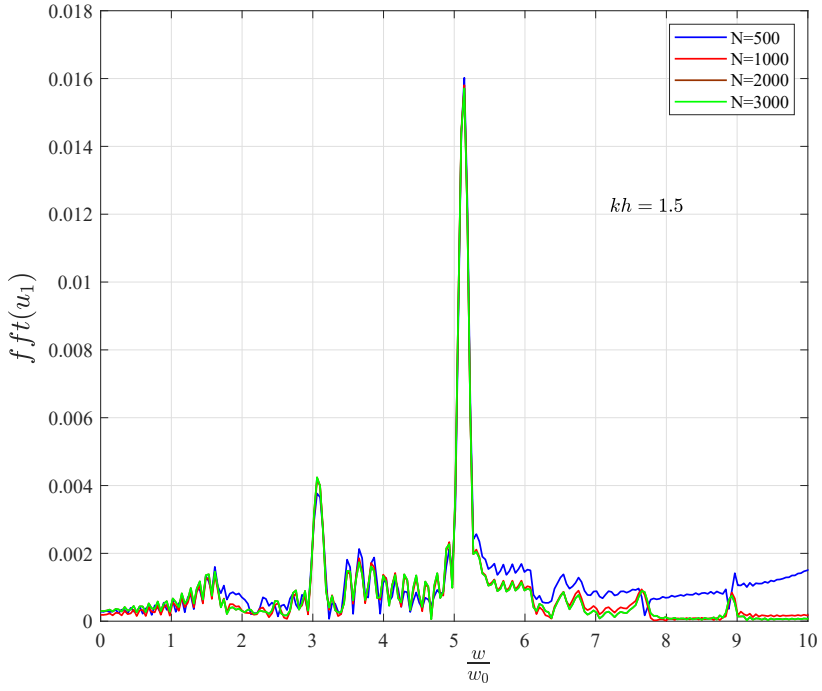

Figure 36: The convergence of frequency spectra with respect to the time-wise terms.

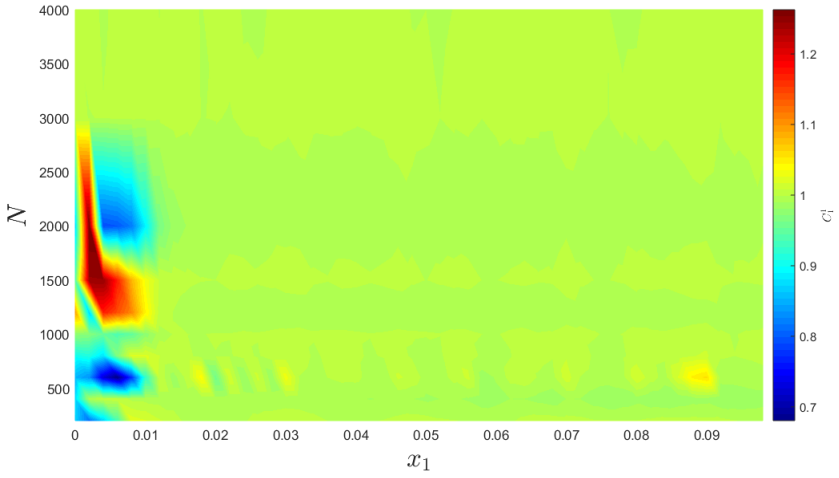

Figure 37: $C_1^1(N, x_1)$ for nodal points at the top of the plate.

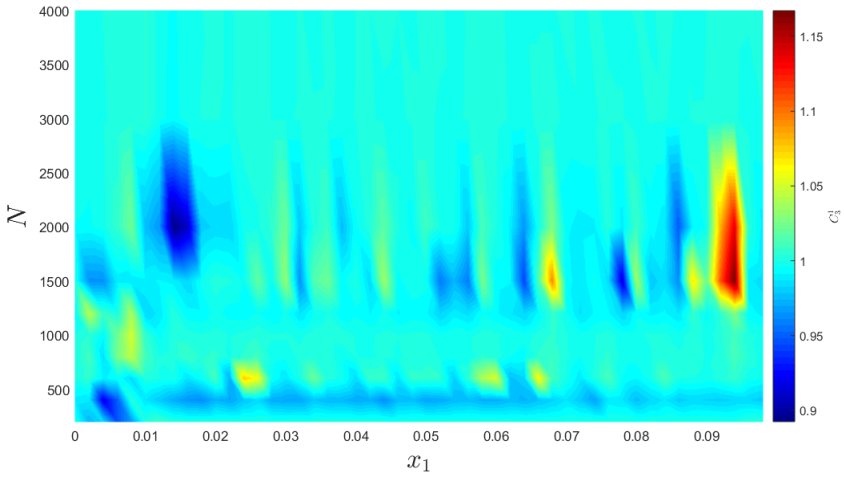

Figure 38: $C_3^1(N, x_1)$ for nodal points at the top of the plate.